Gusev photometric variability as seen from orbit by hrsc/mars-express

A. Jehl, P. Pinet, David Baratoux, Y. Daydou, S. Chevrel, F. Heuripeau, N. Manaud, A. Cord, C. Rosemberg, G. Neukum, et al.

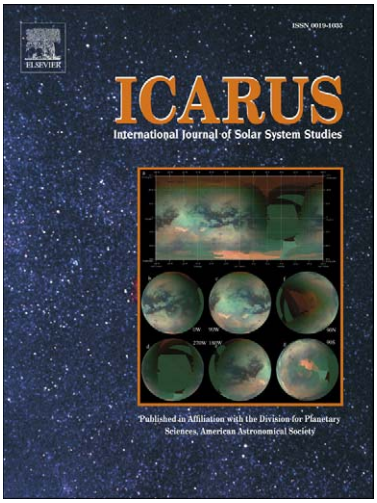

Gusev photometric variability as seen from orbit by hrsc/mars-express

A. Jehl, P. Pinet, D. Baratoux, Y. Daydou, S. Chevrel, F. Heuripeau, N. Manaud, A. Cord, C. Rosemberg, G. Neukum, K. Gwinner, F. Scholten, H. Hoffman, T. Roatsch

PII: S0019-1035(08)00226-1
DOI: 10.1016/j.icarus.2008.05.022
Reference: YICAR 8704

To appear in: *Icarus*

Received date: 22 January 2008
Revised date: 25 April 2008
Accepted date: 29 May 2008

Please cite this article as: A. Jehl, P. Pinet, D. Baratoux, Y. Daydou, S. Chevrel, F. Heuripeau, N. Manaud, A. Cord, C. Rosemberg, G. Neukum, K. Gwinner, F. Scholten, H. Hoffman, T. Roatsch, Gusev photometric variability as seen from orbit by hrsc/mars-express, *Icarus* (2008), doi: 10.1016/j.icarus.2008.05.022

GUSEV PHOTOMETRIC VARIABILITY AS SEEN FROM ORBIT BY HRSC/MARS-EXPRESS

A. Jehl[1], P. Pinet[1], D. Baratoux[1], Y. Daydou[1], S. Chevrel[1], F. Heuripeau[1], N. Manaud[1], A. Cord[1], C. Rosemberg[1], G. Neukum[2], K. Gwinner[3], F. Scholten[3], H. Hoffman[3], T. Roatsch[3] and the HRSC team

[1] UMR 5562/DTP/CNRS/ OMP, Toulouse, France

[2] Freie Universität, Berlin

[3] DLR, Berlin

Mailing address : P. Pinet, UMR 5562/ DTP/ CNRS, Observatoire Midi-Pyrénées, 14, Avenue Edouard Belin, Toulouse, 31400 France

e-mail : pinet@dtp.obs-mip.fr

fax : (33) 561332900

51 pages

7 tables and 19 figures (sent separately)

GUSEV PHOTOMETRIC VARIABILITY AS SEEN BY HRSC

Name : Patrick PINET

Address for editorial correspondence : UMR 5562/ DTP/ CNRS, Observatoire Midi-Pyrénées, 14, Avenue Edouard Belin, Toulouse, 31400 France

Abstract : Minnaert and two-term phase function Hapke models are used to describe the photometric properties of the martian surface using HRSC (High Resolution Stereo Camera) multi-angular observations acquired along the ongoing Mars-Express mission. These observations can be pieced together to derive integrated phase functions over a wide range of phase angles. The photometric diversity at 675nm, as seen from orbit, of the martian surface properties across Gusev is depicted with seven units. Three photometric units widespread across the flanks of Apollinaris Patera flank and the floor of Gusev Crater are identified as having high single scattering albedo with rather forward scattering properties, low to intermediate macroscopic roughness and porous or not compacted powdered surface state as indicated by the opposition parameters. Another unit has the highest single scattering albedo, the smoothest surface in terms of macroscopic roughness, associated with an extremely forward scattering behavior. The opposition parameters are consistent with the presence of transparent particles in the surface powder layer. The distribution of this unit appears quite intermittent across the crater and does not seem to indicate any relationship with a given morphological structure. It may correspond to sparse areas where the structure of the surface dust layer is the most preserved. The most pronounced photometric changes are observed in three units associated with the low-albedo features corresponding to dark wind streaks. These units have a low single scattering albedo, are the most backscattering surfaces across Gusev, have a high surface roughness and present variable surface states as shown by the opposition parameters estimates, consistent with the occurrence of large grains organized in more or less packed layers. Clear differences are seen among these units in terms of opposition effect. While one exhibits typical characteristics for the opposition effect, another appears more unusual in terms of lobe width and the third suggests the occurrence of a packed / compressed / narrow size distribution powder surface. The opposition effect thus appears to play a significant role suggesting that the surface state optical properties across Gusev are strongly

influenced by the porosity and packing characteristics or grain size distribution of the upper layer of the martian soil. The mapping aspect of the investigation is quite useful to get a better sense of the meaning of the observed photometric variations. Indeed, the Hapke modeling suggests that surface organization (surface roughness, packing state, …) is more important than the simple physical characterization of the intrinsic optical properties of the constitutive particles. Given the overall spatial patterns derived from the photometric analysis, the variations, at least for the western and central part of Gusev Crater, are likely partly driven by the prevailing wind regimes, considered to be oriented north-northwest/ south-southeast and disturbing the very upper surface layer. The present photometric results agree with independent investigations based on thermal inertia, reflectance spectroscopy, in situ photometric and microscopic imaging and support the idea of a thin layer of fine-grained dust, being stripped off in the low albedo units to reveal a dark basaltic substrate comprising coarse-grained materials.

Keywords : Mars, surface ; photometry ; regoliths ; radiative transfer

1.Introduction :

More than twenty years ago the importance of linking multispectral observations obtained both from the Viking orbiter and lander multispectral instruments was demonstrated for the purpose of identifying the key components present at the sub-pixel level within the orbital imaging data (Arvidson et al., 1982; Adams et al., 1986). Since then, various observations including telescopic, orbital, and in situ imaging spectroscopic data, and their related interpretations have led to the idea that the martian surface displays heterogeneous optical/spectroscopic properties at different spatial scales. These heterogeneities arise from the geological transitions and geomorphic boundaries, from the physical surface processes responsible for the surface texture caused by transport, erosion and deposition, and/or from the in situ ongoing geochemical processes of alteration and diagenesis likely to occur in the martian soils and subsurface layers.

Optical observation of planetary surfaces is complicated by the surface photometric function and atmospheric scattering, which results in wavelength-dependent limb-darkening profiles (e.g ; Veverka et al., 1978). Indeed, under a given viewing geometry, the reflectivity of the martian surface depends both on the surface composition and physical properties, such as surface roughness, at all spatial scales (e.g., Hapke, 1984 ; Adams and Gillespie, 2006; Mushkin and Gillepsie, 2005, 2006 ; Cord et al., 2007 ; Mc Cord et al., 2007). In the past, despite the progressive development of photometric modeling for addressing the light scattering behavior by the surface (Hapke, 1981, 1984, 1986, 1993, 1999, 2002), the influence of the viewing geometry has generally not been addressed in the interpretation of martian surface spectral variability as observed by telescopic and orbital means (e.g., ISM-Phobos-2, earth-based telescopes, HST (Hubble Space telescope)). The reason for it is the paucity of appropriate data acquired under varying observational conditions (e.g., Erard et al., 1994 ; Mustard and Bell, 1994 ; Kirkland et al., 1997, Bell et al., 1999 ; Johnson et al., 2008).

However, over the years, telescopic and spaceborne photometric observation of planetary regoliths has progressively evolved from whole-disk toward disk-resolved measurements at regional scales (e.g., Geissler and Singer, 1992; DeGrenier and Pinet, 1995; Helfenstein et al., 1996; Simonelli et al, 2000; Warell and Limaye, 2001 ; Pinet and Rosemberg, 2001 ; Clark et al., 2002 ; Warell, 2004; Soderblom et al., 2006), and in the case of Mars, toward in situ studies (e.g., Guinness et al., 1997 ; Johnson et al., 1999 ; Johnson et al., 2006). In particular, during the 1988 opposition, visible near-infrared multispectral imaging data were obtained at the Pic du Midi Observatory in France, and a nearly global coverage of the martian eastern hemisphere, acquired under small phase angles and varying observational geometries conditions, was produced. This dataset offered for the first time the possibility to explore the regional (100-300 km scale) photometric behavior of the martian surface as a function of the wavelength and surface albedo. Given the small phase angle observation conditions, Minnaert's equation was used to approximate the photometric behavior of particulate surface (DeGrenier and Pinet, 1995). The limitations of the Minnaert model are reached for large phase angles and large incidence and emergence (McEwen et al., 1991), so that this function is well suited for the center of the disk observed at opposition. Consequently, only the central parts of the disk images, for which the incidence and emergence are less than 60º, were considered. Generalizing the procedure developed in (DeGrenier and Pinet, 1995) within the common overlap zones existing between successive images in the mosaic, Pinet and Rosemberg (2001) mapped the regional variations of the Minnaert coefficient by minimizing the residual normal reflectance difference of common martian surface elements observed under different viewing geometries, with the derivation of the related geometric albedo. The results indicated that, though the modal value for the Minnaert coefficient k is around 0.75, in general agreement with the literature (e.g., Tejfel et al., 1992 ; Erard, 2000), there exists a wide variability ranging mainly between 0.5 and 1,

with a lower distribution tail comprised between 0.35 and 0.50, more pronounced at 0.91 and 0.98 μm than at 0.73 μm wavelength, apparently associated with the distribution of the low albedo terrains (Pinet and Rosemberg, 2001).

The photometric function of Mars appears increasingly influenced from the visible to near-infrared by the variability of the surface / atmosphere system (e.g., Erard et al., 1994). Several types of mechanisms can be invoked, with the possibility of a large contribution of atmospheric multiple scattering for wavelengths larger than 0.7 micron associated with regional variations of opacity and suspended particles and aerosols in the atmosphere (e.g., Combes et al, 1991; Clancy and Lee, 1991; Erard et al. 1994), obeying Mie scattering (Drossart et al., 1991). However, observations, made at time of 1988 opposition, indicated a low opacity τ (Pinet and Chevrel 1990) indirectly estimated as 0.5 or less at 1 μm. Consequently, in agreement with Regner et al. (1988) and Arvidson et al. (1989), instead of ascribing the observed variability to regional spatial variations of atmosphere opacity, it was concluded that the intrinsic sub-pixel heterogeneity of the martian surface coupled with enhanced contrast might strongly influence the martian photometry in the near-infrared. This sub-pixel heterogeneity of the martian surface in the 0.7 - 1 μm domain could be related to the occurrence of ferric and ferrous absorptions features (e.g.. Pinet and Chevrel 1990 ; Bell et al., 1993; Mustard et al. 1993; Murchie et al. 1993; Martin et al al., 1996; Bell et al., 1997; Erard, 2000) associated with sub-pixel exposed lithology surface units sparsely covered by a variable amount of soil and / or dust particles that are more or less cemented. This would result in variable grain size distributions, responsible for changing surface roughness or texture at sub-pixel scale and contributing to viewing geometry effects (e.g., Fischer and Pieters 1993). These results highlighted the fact that the martian surface photometric properties are complex and generally non Lambertian and have been recently confirmed with

observations in the near-infrared made by PFS (Planetary Fourier Spectrometer) onboard Mars Express (Esposito et al., 2007).

One essential conclusion from these studies was that the detailed interpretation of martian reflectance data should take into account differential photometric effects caused by the combination of observational geometry and the existence of the martian atmosphere with its variable aerosol contribution. Though the martian atmospheric contribution cannot be totally excluded, it was suggested that the martian spectrophotometric properties might be prevalently controlled by the behavior of the particulate surface material (Pinet and Rosemberg, 2001).

To progress any further in our understanding and description of the martian surface photometric behavior (e.g., texture, roughness, porosity, proportion of crystals versus fines) requires multiangular and/or multitemporal spectrophotometric analyses. This ongoing task has been undertaken both in situ and from orbit by, on one hand, appropriate multispectral imaging sensors such as Pancam (IMP (Imager for Mars Pathfinder), MER (Mars Exploration Rover)) and HRSC/Mex (Mars-Express), and on the other hand, by imaging spectroscopy instruments, through dedicated spot pointing observations (OMEGA (Observatoire pour la Minéralogie, l'Etude des Glaces et l'Activité)/Mex) and systematic emission phase function studies (CRISM (Compact Reconnaissance Imaging Spectrometer for Mars)/MRO (Mars Reconnaissance Orbiter)). In order to better interpret the physical and mineralogical properties of the surface at sub-pixel scale, one must address the physics that controls the light interaction processes with soil components. However, these processes are related to electromagnetic energy and its interaction with a particulate interface through a combination of specular reflection, transmission, absorption, diffraction, and multiple scattering from adjacent particles (e.g., Hapke, 1993). The physics of this process is complex and no complete analytical solution has been established so far. A number of semi-empirical

models have been developed for analyzing the bidirectional reflectance data of particulate surfaces based on the scattering and absorption properties of minerals and rocks (e.g., Hapke, 1981, 1986, 1993; 2002 ; Johnson et al., 1992; Hiroi and Pieters, 1994; Shkuratov et al., 1999). The Hapke model, the most frequently employed scattering model, is generally difficult to handle as it requires the knowledge of six parameters, linked with the multiple scattering, the phase function, the opposition effect, and the surface roughness. Its complexity has been discussed against other models (Helfenstein and Veverka, 1987, Geissler and Singer, 1992, Liang and Townshend, 1996; Douté and Schmitt, 1998; Mishchenko et al., 1999; Shkuratov et al., 1999, Poulet et al, 2002). Cord et al. (2003) developed a method to alleviate these limitations in the determination of the global set of Hapke parameters, when dealing with a set of angular conditions representative of the usual range of observation in planetary exploration (phase angle between 20° and 120°) for spaceborne optical instruments. This approach is founded on a genetic algorithm ; the whole set of Hapke parameters is treated simultaneously without any a priori assumptions. It limits the risk of meeting a local minimum in comparison to other methods of inversion, and the stability and repeatability of the determination are improved.

Beyond its application to laboratory studies (e.g., McGuire and Hapke, 1995 ; Cord et al., 2003 ; Shepard and Helfenstein, 2007), Hapke modeling has been implemented so far on a limited number of terrestrial and martian in situ photometric observations (e.g., Shepard et al., 1993 ; Guinness et al., 1997; Johnson et al., 1999, Johnson et al., 2006). A few exploratory studies excepted (Regner, 1988 ; Arvidson et al., 1989 ; Geissler and Singer, 1992), it has not yet been extensively tested on Mars with well-documented orbital datasets. Only quite recently such a dataset has been produced with the multi-angular High resolution Stereo Camera (HRSC) instrument on-board Mars-Express. It is the purpose of this paper to explore by means of different photometric modeling approaches (i.e., Minnaert, Hapke)

whether this orbital information can be used for characterizing the martian surface photometric behavior, at rather high spatial resolution (in the range of a few hundred meters) and linked to the various investigated geologic surfaces, in a consistent manner with the photometric observations available from in situ observations (e.g., Arvidson et al., 1989; Strickland, 1989, Guinness et al., 1997; Johnson et al., 1999, Johnson et al., 2006). Accordingly, the focus of the paper is placed on Gusev Crater for which a wealth of information is available, as a result of the in situ exploration carried out by the rover MER *Spirit* spacecraft (e.g., Squyres et al., 2004 ; Bell et al., 2004 ; Arvidson et al., 2004, 2006; Johnson et al., 2006).

2. HRSC Data Set and Processing

One of the new investigations from orbit that can be addressed with the multi-angular HRSC dataset generated with the nadir-looking, stereo and photometric channels, is to derive the surface photometric characteristics for mapping the variation of the soil/bedrock physical properties of Mars, and to relate them to the spectroscopic and thermal observations produced by OMEGA, TES and THEMIS instruments. HRSC is a push-broom imaging system. It contains 9 parallel CCD-line detectors; nominally, their linear fields of view are oriented normal to the orbit track; an image is built up by repeatedly reading out each array as the spacecraft moves over the surface and the field of view scans the surface. Each detector array views the scene at a different angle from forward to aft of nadir so that each detector views a different line in the scene at any instant of time. Nine detectors consecutively scan the same surface area producing nine overlapping images. Five of the nine detectors have the same panchromatic filters. Based on technical specifications of the laboratory calibration equipment and on experiences and investigations carried out by the German Aerospace

Center (DLR) on the data, the reflectance uncertainty of the panchromatic channels can be estimated as less or equal to 3% (personal communication with the HRSC experiment team). These detectors are usually referenced as nadir channel (nominally directed toward nadir), two photometric channels (directed 12.9° in both directions from nadir), and two stereo channels (directed 18.9° from nadir). Since they have different emission and phase angles, this set of five overlapping images can potentially be used to extract photometric information (Neukum, ESA SP1240 ; McCord et al., 2007). However, this possibility presents some limitations due to the narrow range of photometric angles sampled. As a matter of fact, a single orbit HRSC image set does not contain enough information for describing the photometric function (see Pinet et al., 2005, Jehl et al., 2006, Pinet et al., 2006).

In order to compensate for the limited number of observational geometries associated with one HRSC acquisition, observations from several overlapping strips acquired at different times along the mission must be combined in order to span as much as possible the phase angle domain (Pinet et al., 2005 ; Jehl et al., 2006). The region under study is the Gusev Crater and the south flank of Apollinaris Patera (Figs. 1 and 2) for which 10 overlapping strips have been obtained by Mars Express in 2 years orbiting around Mars (Tables 1 and 2), with 2 orbits (24 and 72) at low phase angle ($g<50°$;$i\sim30°$), 2 orbits (637 and 648) at high phase angle ($g>60°$; associated with dawn illumination conditions, $i\sim80°$) and 6 additional orbits (987, 1879, 2249, 2271, 2685, 2729) with varied geometric conditions). The HRSC observations have been acquired with a compression ratio varying between 5 and 15 and initial binning modes comprised between 1 and 4. In the following, HRSC data are binned at 1.6 km / pixel and orthorectified with the HRSC DTM October 2005 version (Scholten et al., 2005) to correct for mis-registration and minimize compression effects. The HRSC regional elevation and slope maps, produced at 400m/pixel resolution from orbit 2271 (Fig. 3), are considered to be the best product for this area. However, DTM residual noise causes yet some

imperfection and advanced DTM products should be implemented for addressing studies at higher spatial resolution (e.g., Gwinner et al., 2005 , 2007 ; Jaumann et al, 2007 ; Lohse et al., 2006; Spiegel et al. 2007 ; Heipke et al., in press). With very oblique illumination conditions, observational limitations are the shadows caused by the local relief (see Fig. 2) and decreased S/N ratio. Taking advantage of the extended phase domain ranging up to 95°, associated with a diversity of illumination conditions (Figs. 1 and 2), the Hapke inversion procedure developed and tested on experimental data (Cord et al., 2003), employing a double Henyey-Greenstein function, has been used to model the surface photometric properties (Jehl et al., 2006).

However, in a first step, a much simpler photometric analysis has been performed relying on the Minnaert phenomenological modeling. It is indeed worth applying this to rather high resolution data, at a spatial scale related to geomorphic features and albedo units seen across the scene and for which the in situ knowledge is available. It has never been done in the past and it is the purpose of the next section to explore and document the existing links between earlier photometric results (i.e., normal albedo and Minnaert parameter), produced at regional / global scales and the observed local variations, and to assess the degree of non Lambertian behavior of the martian optical response, at local spatial scales in the range of a few hundred meters to one kilometer.

3. Minnaert results at Gusev

Initially developed by Minnaert (1941), the Minnaert function has been widely used for characterizing the surface photometry of the moon, and more recently that of mercury and small planetary bodies (e.g., Simonelli et al., 2000; Warell and Limaye, 2001). It has also been used to model the martian photometric properties from orbital and telescopic datasets

(e.g., Degrenier and Pinet, 1995; Erard, 2000; Esposito et al., 2007). It can be considered as a generalization of the Lambert model and is able to describe the scattering properties of most particulate materials and surfaces, especially at low phase angles (Degrenier and Pinet, 1995). For a given wavelength λ, the reflectance depends on the solar phase g, emission e and incidence i angles as follows:

$$r \cos e = r_0(g, \lambda) (\cos i \cos e)^{k(g, \lambda)} , \quad (1)$$

where r is the bidirectional reflectance, $r_0(g, \lambda)$ is the Minnaert albedo. Equation (1) gives the dependence of reflectance upon the physical state of the surface through the k parameter. In the case of disk-integrated observations, this quantity, called the Minnaert parameter, usually varies from 0 to 1 as a function of phase angle and wavelength and describes the limb-darkening effect. Typical values of this parameter on mineral samples and planetary bodies range from 0.5 to 1. The case k=0 corresponds to cosine limb-darkening; a Lambert surface would give k=1; a specular reflector would correspond to $k \to \infty$. The full Moon has no limb effect, so that k=0.5 (Helfenstein and Veverka, 1987). The value of k is related to multiple scattering, hence to texture or roughness, and can be sensitive to atmospheric scattering in the presence of an atmosphere.

Relying on the most recent studies (Esposito et al., 2007), the choice has been made here to limit the angular range such as the incidence, emergence and phase angles be less than 60°. Applying this condition to the HRSC dataset leaves however a significant number of geometric configurations (typically on the order of 10 to 15). The local variations of the Minnaert parameters (r_0 and k) are mapped through a root-mean square approach by minimizing the residual normal reflectance difference of common martian surface elements observed under different viewing geometries, similar to the approach used by DeGrenier and

Pinet (1995); the score, defined either as the absolute or the relative quadratic residuals (Fig. 4), provides an assessment of the quality of the fit. The relative residuals are defined as the quadratic residuals from the sum of the observed-modeled difference divided by the reflectance of each observation. It is thus a quantity which is independent from the variation of reflectance between bright and dark terrains and enables us to compare the intrinsic quality of the fit, whatever the reflectance level. Typical values around 4-7% (Fig. 4b) demonstrate the suitability of Minnaert modeling under the considered range of geometries. The uncertainties assessed for the cases of a dark, then a bright terrain are in the range of 0.05 for k on both terrains, and respectively 0.01 to 0.02 on r_0.

In a first step, the Minnaert analysis has been used to model specific regions of interest (referred to as ROIs in the following) distributed across Gusev, spanning both the observed albedo range and terrain types, as based on the morphology, thermal and in situ observations. Four ROIs are considered and referred to as red, cyan, yellow, green (see Fig. 1 for their location within Gusev Crater and Table 3 for their thermophysical characteristics). They correspond to bright terrains with low thermal inertia (in red), bright terrains with intermediate thermal inertia (in cyan), dark terrains with low albedo and intermediate thermal inertia (in yellow), dark terrains with intermediate albedo and high thermal inertia terrain (in green) and respectively belong to the Plains Materials (WRt), Transitional Plains Materials (PLt), Low Albedo (LAt), High Thermal inertia (HTIt) thermophysical units (Jakovsky et al., 2006; Milam et al, 2003; Martinez-Alonso et al., 2005). Based on these studies, WRt has properties consistent with those of an indurated surface, covered mostly in fine-grained sand. PLt is interpreted as a surface dominated by coarse sand, involving coarse grains, rocks and bedrock. LAt is dominated by a surface interpreted as indurated materials, coarse particles, exposed rocks or bedrock, and devoid of unconsolidated fine materials. Milam et al. (2003) proposes the surface to be mainly covered by medium-grained sand. HTIt is viewed as a

surface composed of coarse sand to granule particles, exposed rocks or bedrock, may include crater ejecta. It is interpreted as materials of basaltic composition, differentiating younger lava flows and older deposits (Martin-Alonso et al., 2005; Jakovsky et al., 2006). The Minnaert parameters estimates produced for the four selected ROIs (red associated with WRt, cyan with PLt, yellow with LAt, green with HTIt) considered here show substantial variations as shown in Fig. 6 which strongly suggest that the surface physical properties are influencing the photometric response. However, no obvious difference is observed between the red and cyan ROIs, respectively represented by a cross and a star in Fig. 6 while the yellow (square symbol) and green (diamond symbol) ROIs behave differently between them and with respect to the red and cyan ROIs.

A regional map of the Minnaert variations across the region of study is then produced. The spatial variations across Gusev Crater resulting from the Minnaert modeling are explored at 400 m/pixel resolution and displayed on Fig. 5 (results with no filtering on Figs. 5b and 5d). It is worth pointing out that an increase in the relative quadratic residuals is mainly observed for pixels with local slopes exceeding 3° which have thus been discarded in the mapping (spatial filtering based on local slopes). Consequently, on Figs. 5c and 5e, only the well-modeled areas, i.e. with low residuals less than 7% (Figs. 5a and 4b), have been mapped. As a result, the graph shown in Fig. 6 demonstrates the overall relationship existing between k and r_0, with k generally varying between 0.5 and 1 as revealed by the k histogram. The histograms show that, for the region under study, the modal k value is 0.9 and the modal normal albedo is 0.3. Following earlier studies at lower spatial resolution, one notes a general trend showing that the Minnaert exponent increases from 0.5 to 1 when the albedo increases, though not in a simple linear way (e.g., DeGrenier and Pinet, 1995; Pinet and Rosemberg, 2001; Soderblom et al., 2006; Esposito et al., 2007). As shown in Fig. 7, the same trend is observed when considering a region with a resolution of 100m / pixel in the vicinity of

Columbia Hills, the Minnaert variations clearly delineating the pattern of dark and bright transitions. For both Bonneville and El Dorado dark patches, we obtain low k, 0.46 and 0.37 respectively, and Minnaert albedo values, 0.20 and 0.19 respectively, while in the surrounding intermediate bright plains, we find k= 0.7-0.9 and r_0=0.25 - 0.30. On Fig. 7c, it is quite interesting to note at 100-m resolution the local residuals increase at the periphery of the dark streak region consistent with the occurrence of local surface changes (Greeley et al., 2006) during the 2-year period of observation.

It appears that the most obvious relationship between k and r_0 is the association of low k values with low albedo corresponding to high thermal inertia values. A striking result is the fact that the low k values map out very conspicuously the low albedo units, with the lowest estimates ranging around 0.46- 0.50 in the center of the dark patches such as the one where Spirit has landed, in association with a r_0 estimate of 0.19-0.20. For intermediate to high albedo terrains, a general increase is noted, but the distribution of k values is more scattered and not strictly linear. This result highlights the fact that photometric variations are clearly evidenced at local scale, with the same general behavior than previously shown at regional scale (e.g., DeGrenier and Pinet, 1995; Esposito et al., 2007). It demonstrates that in the observed system coupling the martian surface and atmosphere, it is indeed the surface properties which control the observed photometric response when the atmosphere is relatively transparent ($\tau < 0.8$ or so). It suggests that, under those conditions of observation (low τ and low i, e, g < 60°), the atmospheric variability (aerosol distribution) cannot account for the observed lateral photometric differences.

The results obtained with the Minnaert function show that the general case for the martian surface is to behave in a non Lambertian way, with bright terrains having a Minnaert coefficient in the range of 0.7-1, while lower albedo terrains have a lower k comprised between 0.45 and 0.7. It means that the bright martian units behave in a more Lambertian

way than the dark ones, which are more lunar like. While the Minnaert coefficient is known to be phase angle dependent (e.g., Soderblom et al., 2006), it is worth noting that we can derive its estimate, considering a fairly wide range of phase angles up to 60°, with quite low residuals generally less than 0.02 in reflectance, corresponding to relative residuals less than 6% (Figs. 4a and 4b). It suggests that one can make use of the multiangular multi-orbits HRSC dataset acquired between 2004 and 2006 for photometric investigations.

4. Implementation and testing of Hapke photometric modeling :

Accordingly, the next logical step was to explore the photometric variability by means of the Hapke function (Hapke, 1993), considering a 2-term Henyey-Greenstein (HG2) phase function (Soderblom et al., 2006 ; Johnson et al., 2006). The model used here includes the single scattering albedo (*w)*, the macroscopic roughness ($\bar{\theta}$), representing the average of surface facet tilts at scales from the wavelength of light to the centimeter-scale (e.g., Helfenstein and Shepard, 1999 , 2003 ; Cord et al., 2003 ; 2005), the opposition effect width (h) and magnitude (B0) and a 2-term HG phase function p(g) (Eq. 2), with b representing the asymmetry parameter (0<b<1) and c the backward scattering fraction (0<c<1) such as :

$$p(g) = \frac{c(1-b^2)}{(1+2b\cos g+b^2)^{1.5}} + \frac{(1-c)(1-b^2)}{(1-2b\cos g+b^2)^{1.5}}, \qquad (2)$$

The parameter h (0<h<1) is physically related to porosity and particle size distribution. Less porous materials or with little variation in the constitutive particles size have large values of h. B0 parameter is related to the opacity of particles, a value of 1.0 meaning that all light is

scattered at the surface and the particle is consequently opaque. From their study of artificial particle types, (McGuire and Hapke, 1995) have proposed that the (b, c) parameters vary from the situation of forward scattering associated with a low large lobe of diffusion (large b, small c), reflecting the case of smooth clear spheres, to the situation of pronounced backscattering associated with a high narrow lobe (small b, large c), as seen in the case of particles presenting rough surfaces, microcracks or inclusions. However, a recent experimental study (Shepard and Helfenstein, 2007) suggests that the interpretation of the results returned by the Hapke modeling is more complex.

In order to implement and test this model on a varied dataset, we consider 10 representative ROIs (Fig. 8) which include the 4 previously selected ROIs and encompass a variety of surface types across Gusev Crater and Apollinaris south flank. As said before, Hapke modeling has obvious shortcomings, in particular when used in an inverse approach; we have set up in this paper a procedure based on a genetic algorithm which produces results with both a robust physical and statistical meaning.

This is implemented and discussed for the 10 cases mentioned above. Figure 9 shows 4 examples, displayed on polar diagrams (left and middle columns), of the geometry of the available observations (radial distance : incidence, emission angles ; polar angle : azimuth), with the right column displaying the phase function information expressed in reflectance factor (REFF = π.r/ cos (i), with i : incidence angle) (see Hapke, 1993, p. 262), in order to emphasize the differences in the overall shape, in particular at large phase angles (i.e., g> 60°). These diagrams highlight the fact that, though the photometric coverage is not complete, observations have been carried out under quite varied geometries, including observations out of the principal plane and with forward and backward scattering situations.

Differently from Johnson et al. (2006), no attempt has been made at separating the

atmospheric contribution from the surface one and the Hapke inversion is applied to the global signal retrieved by HRSC, with the idea of assessing whether the photometric products so derived would be consistent or not with the in situ results from Viking, Pathfinder, MER.

The case for HRSC observations differs from that of Pancam in situ observations. While Pancam observations are all acquired with a large emission angle e > 45° (e.g., Johnson et al., 2006), HRSC data are generally not far from nadir conditions, with e < 30°. What matters is, thus, both the atmospheric opacity and the large incidence angles. The most critical situation in our dataset is encountered for the orbits 637, 648, and 1879, with i around 75-80°. Fortunately, for orbits 637 and 648, the opacity is quite low ($\tau \sim 0.3$) and under these conditions, the atmospheric contribution should not exceed 0.02 -0.03 in REFF when e < 30° (simulations performed by Vincendon M., private communication). However, a number of tests performed on the dataset has shown that orbit 1879 was photometrically inconsistent with the other orbital datasets and it has thus been discarded in the following. Looking at Table 1, one notes that the atmospheric opacity associated with this observation was quite high indeed, in the range of 1.3, while all other observations were performed with τ ranging between 0.3 and 0.9, which is the most frequent situation in the Vis-near IR spectral domain as measured by Pancam (Lemmon et al., 2004 and 2006) and TES (Clancy et al., 2003). No exact quantification can be provided at the present time and it is possible that the lack of atmospheric correction may result in a slight systematic overestimation of the amount of forward scattering intrinsically associated with the surface properties.

The results of the Hapke inversion by means of the genetic algorithm are shown on Fig. 10. These graphs show the first 200 best solutions as a function of the score, defined as the RMS (Root-Mean Square) residuals between the observed and the modeled reflectance under all the considered viewing geometry configurations.

The Hapke parameter estimates are given in blue for *w*, in green for $\overline{\theta}$, in black and red for

the phase function parameters b and c respectively, and in orange and pink for the opposition parameters B0 and h. On the left-hand side of the graph, the histogram shows whether the parameter determination is well or poorly defined. On the bottom part of the graph, the downward-pointing histogram shows how the solutions are distributed as the residuals increase. The results show that in all cases *w* is well defined. For $\overline{\theta}$, the distribution may be a bit more scattered for some examples (e.g., Red ROI (Fig. 10a)). The b and c parameters, as discussed earlier (e.g., Helfenstein and Veverka, 1987, 1989 ; Cord et al., 2003 ; Johnson et al., 2006 ; Baratoux et al., 2006 ; Shepard and Helfenstein, 2007), are strongly coupled, with c sometimes poorly constrained (e.g., (Fig. 10d)). Despite our effort to expand the phase angle domain with the consideration of multi-orbit observations, only a limited number of geometries are available and non-unique solutions may be found (Jehl et al., 2006; Pinet et al., 2006). Figure 10 shows that the best fit solution (i.e., corresponding to the lowest residuals), provided by the genetic algorithm, has to be balanced with its statistical occurrence (see also Johnson et al., 2006). To illustrate this point, we give on Figs. 11, 12 and 13, a rendition of the parameters' distribution for the 30 best estimates. One sees that depending on the considered case, the clustering of the solutions can be sharp or more diffuse and this affects the standard deviation (see Table 4) used here as an uncertainty on the parameter estimate. This is the reason why in the following, the Hapke parameters' estimates we propose correspond to the mean from the 30 best solutions ranked as a function of the residuals, as a number of tests that we performed has shown this estimate (and its associated standard deviation) to be both more robust and representative of the distribution of the results given by the inversion than the best fit solution. The estimates of the Hapke parameters ($w, \overline{\vartheta}$, b, c, B0, h), their standard deviation and the absolute and relative residuals of the photometric modeling are given in Table 4.

With this set of Hapke parameters, following Johnson et al. (2006), the bidirectional

reflectance distribution function (BRDF) is plotted against the full set of HRSC observations (at the exclusion of orbit 1879) for the 10 investigated ROIs and the difference between model and observation is displayed below for each geometric configuration (Fig. 14). One sees that the Hapke function does a rather good work fitting each observation contributing to the integrated phase function. Indeed, the relative residual is quite frequently better than 5-7%, corresponding to an absolute residual less than 0.02 in REFF or 0.006 in BRDF (Table 4).

The suite of ROIs investigated here present b-c coupled variations describing the L-shape domain described by McGuire and Hapke (1995). It is worth pointing out that the ROIs (in green and yellow) having the highest surface roughness ($\overline{\theta}$ ~ 14-17°) among the 10 considered, are relatively the most backscattering ones (c ~ 0.4 - 0.5), and have the lowest single albedo estimates (w ~ 0.69-0.74).

B0 and h are seen to vary significantly from one ROI to another; however, the most frequent solution, in agreement with the results found in situ at Spirit by Pancam photometric observations (Johnson et al. , 2006), gives B0 ranging between 0.8 and 1, suggesting that almost all the light is scattered at the very surface and the particles or aggregates of particles are opaque, with h ranging between 0.05 and 0.25. The parameter h is physically related to porosity and particle size distribution. To give an idea, the case of the lunar regolith is characterized by B0=1 and h=0.065 while a surface composed of close-packed powder with a narrow size distribution will have h=0.26 (Hapke, 1993, p. 226).

The modeling includes an opposition phase function taking into account the SHOE (Shadow-Hiding Opposition Effect) and CBOE (Coherent-Backscatter Opposition Effect) effects, the two of them contributing to a sharp surge in brightness around zero phase angle, with a typical half-width of 5 to 10° (Hapke, 1993). We perform a critical assessment and analyze the results which are produced when ignoring the opposition effect contribution as the

viewing geometry conditions may vary from one pixel to another across the image and not all regions have well-defined phase functions at low phase angles. B0 and h parameters are thus set to 0 and only HRSC measurements corresponding to phase angles larger than 20° are considered. This usually means that 3 observations are discarded. The results of the inversion applied to the 10 ROIs discussed earlier are given in Table 5.

For the majority of the considered areas, the case of Hapke inversion ignoring the opposition effect with a restricted phase angle domain shows that the *w*, b, c, $\overline{\theta}$ estimates are usually not much modified (see for comparison Tables 4 and 5). However, in the case of the purple and yellow ROIs, we observe mainly changes in b, $\overline{\theta}$ and/or *w*. In the cyan case, the inversion is likely underconstrained, reflecting the lack of low phase angles < 10° (see Fig. 9c). For the yellow ROI, the single scattering estimate *w* is clearly more realistic when one includes the opposition effect, but the h estimate is unusual (h= 0.89), suggesting then a very particular surface state possibly affected by a packing effect or presenting a layer with a narrow particle size range.

The present analysis of selected ROIs across the scene has shown that one can generally retrieve realistic photometric estimates for the complete set of Hapke parameters (i.e., 6 in the case of the HG2 Henyey-Greenstein function) from the HRSC data presented in this work. This detailed assessment prompts us to extend the study toward a photometric mapping.

5. Gusev and Apollinaris Patera photometric mapping :

The derivation of the Hapke parameters following this approach has thus been extended to the total coverage over Gusev Crater and Apollinaris southern flank, with a 1.6x1.6 km^2 resolution. The map of the relative residuals (root-mean square) is given on Fig. 15a and the corresponding histogram is shown on Fig. 16. One notes that the residuals increase according

to a spatial pattern which mimics the local slope map (Fig. 3), depicting in particular the edges of the crater. The corresponding threshold is around 8% on the histogram (Fig. 16). Taking this value as a rejection criterion, we keep only the pixels (i.e., about 80% of the coverage) for which the residuals are less than this threshold and look at the distribution of the Hapke parameters on Figs. 15b, c, d, e, f, g. The single scattering albedo determination at 675 nm made from HRSC data agrees quite well with in situ Pancam estimates (Johnson et al., 2006)), with a range of albedos mainly comprised between 0.67 and 0.85. The macroscopic roughness estimates range between 0 and 20° while the b and c phase function parameters lie respectively in the 0.05-0.65 and 0.02-0.6 domains. However, for a limited part of the pixels population, the photometric modeling produces very high b estimates, beyond 0.9 associated with extremely high *w* estimates (> 0.9) and low $\overline{\theta}$ estimates (<7-8°) (see Figs. 15.b, d, e). One notes that the corresponding opposition parameters h, B0 for these areas present unusual values with both of them in the range of 0.4 - 0.5. The terrains presenting this trend are represented in red in Fig. 15b. Though we are skeptical with these results, we also notice some similarities with the case of glossy materials described with the terrestrial Pisgah basalts by Guinness et al. (1997), and with the derivation of the Hapke scattering parameters for the MER Spirit Gray rocks at Sol 13 (Johnson et al., 2006). However, given the anomalous nature of these results, a masking has been applied on the b estimates so that the pixels with b > 0.9 are discarded. This corresponds to about 15% of the region under study.

We then plot on Fig. 17 the histogram distribution corresponding to each Hapke parameter and its associated standard deviation derived from the 30 best solutions. A large proportion of the pixels analyzed in the image present well-determined estimates for b, c, $\overline{\theta}$, *w*. As an example, 80% of the population has a b estimate with a deviation less than 0.02, a c estimate with a deviation less than 0.03, a *w* estimate with a deviation less than 0.008, a $\overline{\theta}$ estimate

with a deviation less than 3°. For the opposition parameters h and B0, the corresponding standard deviations are larger, respectively on the order of 0.1 and 0.18. However, the parameter distributions appear quite realistic with the bulk of the solutions less than 0.25 for h and more than 0.8 for B0 (see Fig. 17). While eolian processes clearly dominate present-day modifications of the surface (Greeley et al., 2006), in agreement with the increase in local residuals increase noted at the periphery of the dark streak region when analyzed at 100-m resolution (Fig. 7c), the low residuals associated with the present photometric inversion, performed at 1.6 km per pixel, suggest a relative stability of the average surface optical properties. This result appears valid in the time frame of the considered 2-year period 2004-2006.

Owing to the very different spatial resolution of this investigation versus the in situ analysis performed at Gusev with Pancam, and to the notion of multispectral classification of rocks and soils used to carry out the Pancam photometry studies on distinct units (e.g., gray rocks, red rocks, bright soils, dark soils, …) (Johnson et al., 2006), a direct comparison between the present results and those from Pancam observations cannot be made in a straightforward manner. However, comparing our results obtained at 675 nm (HRSC visible channel) with Pancam results obtained at 753 nm show that the range of variation found here for each parameter (Fig. 17) is quite consistent with the estimates reached by Johnson et al. (2006). This is particularly true for the single albedo ranging between 0.69 - 0.87, the surface roughness comprised between 0 and 20°, and the lobe width generally ranging below 0.25. For the phase function parameters b and c, an overall agreement is also found but one must keep in mind that our results reflect an average estimate based on the 30 best solutions which tend to reduce the range of variation, in particular for the very backscattering cases as demonstrated in Fig. 11d. We note for instance that while our c estimates are < 0.6, if only the best or 10 best solution(s) (Johnson et al., 2006) are considered, higher c values (between

0.6 and 0.8) are obtained. One must also keep in mind that Pancam is able to sample much larger phase angles than HRSC. This may cause differences between the HG2 parameters constrained here and those of Johnson et al. (2006).

It is also worth pointing out that in both studies (Pancam and HRSC), the amplitude B0 of the opposition lobe is the parameter which is the least constrained, with its most frequent values comprised in our HRSC analysis between 0.8 and 1 (see Figs.17.k and l).

6. Derivation of photometric units across Gusev and Apollinaris Patera :

Our final objective was to characterize and define photometric units within Gusev and over Apollinaris Patera, and attempt to put these units in relation with different types of materials characterized by their thermophysical and/or surface properties as described by other techniques (e.g., thermal infrared, in situ optical (Pancam) and texture analyses (MI)). A multivariate statistical analysis (PCA: principal components analysis) allows determination of photometric types within the population of solutions kept (see section 5; application of a rejection criterion (residuals > 8%) and exclusion of pixels with an anomalous photometric behavior (b > 0.9)). This procedure selects the most representative endmembers in terms of photometric properties and spatial distribution, from which a regional photometric map can be established. We used a dimensionless dataset for the PCA analysis, i.e., centered coordinates normalized for each photometric parameter by the standard deviation of the distribution. This means that the (0,0) coordinates in the PCA diagrams correspond to the barycenter point for the whole population. Absolute photometric quantities can be recalculated from these data (Tables 6 and 7) (see Pinet et al. 2000 and Chevrel et al. 2002 for details about this method from previous applications). The principal axes of variation (defined by the eigenvectors of the correlation matrix of the population) are ranked according

to their decreasing explained variance (respectively bearing 52, 18.9, 17.9, 6.6, 2.6 and 2%). In the present analysis, the topological study of the statistical data cloud projected along the three first principal axes representing 89% of the total variance allows the identification of seven different clusters or domains, shown on Fig. 18. Each domain corresponds to a homogeneous photometric population characterizing a distinct photometric type. These seven units (shown in yellow, green, magenta, orchid, dark-blue, cyan, and orange), are plotted in Fig. 18a. These units are projected on the graphs successively plotting c versus b, $\overline{\theta}$ as a function of *w*, and a third plot describing the opposition effect parameters and displaying B0 as a function of h. The mean and standard deviation estimates of the photometric quantities associated with these units are given in Table 6 and displayed in Fig. 18.

Three units, shown in cyan, dark-blue and orchid, are present on both Apollinaris Patera flank and across Gusev Crater floor. These three photometric units present the same *w* with rather forward scattering properties (high b, low c), low to intermediate surface roughness (cyan, dark-blue vs rougher orchid) and porous or not compacted powdered surface state, or one with less uniform grain size distribution (h low, B0 : 0.7-0.9). The dark-blue unit can be distinguished from the cyan unit only by its B0 amplitude (B0=0.91) consistent with the presence of more opaque particles constitutive of the surface than in the orchid (B0=0.82) and cyan (B0=0.73) units. These units are widespread across the crater floor and Apollinaris.

The unit that has the highest single scattering albedo, shown in orange, is the smoothest surface in terms of macroscopic roughness, associated with an extremely forward scattering behavior. The opposition parameters are consistent with the presence of transparent particles in the surface powder layer. The distribution of this unit appears quite intermittent across the crater floor and does not seem to indicate any relationship with a given morphological structure. It may correspond to sparse areas where the structure of the surface dust layer is the

most preserved.

Three units, shown in yellow, green and magenta, are all associated with low-albedo features and accordingly, have a lower single scattering albedo and rather high surface roughness estimates ($\overline{\theta}$ ~ 14-18°) . The yellow and green units present a backscattering behavior larger than that of the magenta unit. Clear differences are also seen among these units in terms of opposition effect. While the green unit exhibits typical characteristics (narrow width (h=0.13), large amplitude (B0=0.85)), the magenta unit appears more unusual in terms of lobe width (h=0.30), and the yellow unit is atypical with B0=0.73 and h= 0.75, suggesting the occurrence of a packed / compressed / narrow size distribution powder particulate surface. The photometric behavior for the magenta unit supports and provides some physical grounds for the detection of a local photometric anomaly by Kreslavsky et al. (2006). To go further in the physical understanding, one needs to explore the relationships between the photometric variations among the three low-albedo units depicted here, and the variations between the LA (low albedo), HTIR (high thermal inertia rough) and HTIS (high thermal inertia smooth) thermophysical units derived from the thermal data of Martinez-Alonso et al. (2005).

We note that five out of seven of the units described above (cyan, dark-blue, orchid, yellow, green) present the same photometric behavior as five out of the ten individual ROIs analyzed in section 4 and represented with the same color. Given the extensive assessment performed for these areas in section 4 on the implementation of Hapke model (Figs. 10, 11, 12, 13, 14), we feel confident with the definition of the present units based on the Hapke parameters estimates.

The representation of the same photometric clusters (Fig. 19 and Table 7) is also produced when considering a phase function truncated below 20° phase angle and thus neglecting the opposition effect (h=B0=0). The “orchid” unit is scattered across the parametric space; the same occurs to less an extent to the other clusters and the proposed classification is no longer

valid. This demonstrates that the opposition effect plays a significant role in the photometric properties of the surface, suggesting that the surface state optical properties across Gusev are strongly influenced by the porosity and packing characteristics, and/ or grain size distribution of the upper layer of the martian regolith, not excluding possible particle opacity effects related to B0.

It is worth recalling that the TES albedo values for the floor of Gusev range from <0.17 to 0.26 while the dust cover index (DCI) values range from <0.93 to 0.97. Such values are indicative of surfaces that range from dust-covered to dust-free (Ruff and Christensen, 2002). The thermal inertia values, which range from <150 to 500 S.I., indicate that although dust may be present, it is not thick enough to fully obscure the thermal signature of the underlying substrate (Christensen et al., 2005). Recent results produced from Pancam in situ spectral analysis (Farrand et al., 2006) and from combined analyses of OMEGA and Spirit data (Lichtenberg et al., 2007) show that the surface of the Gusev Crater plains is dominated by nanophase iron-oxide-rich dust deposits partially obscuring weakly-altered basaltic sands. While the dust cover may be thick enough to mask the visible-near-infrared spectral signature of the underlying basaltic sands, it is generally not thick enough to influence the thermal signature and consequently should be less than 1 cm thick (Lichtenberg et al., 2007).

The lowest-albedo, least-dusty material exhibits TES spectral properties similar to Surface Type 1 (basalt) while other units appear to be obscured by dust (Milam et al., 2003). However, from the THEMIS IR and VIS data analysis, the floor of Gusev displays temperature variations that are independent of topography. For instance, the relatively low albedo prominent streaks seen in visible images and oriented NNW- SSE are warmer in the day by several degrees than the rest of the crater floor. At high resolution, these features are composed of small, superimposed, sub-parallel streaks that clearly are eolian in origin. The fact that the streaks are nearly indiscernible in nighttime observations tend to support the idea

that a thin layer of bright, fine-grained dust has been stripped off to reveal a darker uniform substrate (Christensen et al., 2005).

Our present photometric results reached from both Minnaert and Hapke modeling support this view with the most pronounced photometric variability associated with the yellow, magenta and green units corresponding to the low-albedo features. These three units have a low single scattering albedo, are the most backscattering surfaces across Gusev and Apollinaris, have a high surface roughness and present variable surface states as shown by the opposition parameter estimates discussed above, consistent with the occurrence of large basaltic sand grains organized in more or less packed layers. In this respect, one recalls that MI images (Herkenhoff et al., 2004 ; Foley et al, 2005), acquired inside a dust devil track (Sol 39), on the contact of the dust devil track and the plains (Sol 52), and outside of the dust devil track (Sol 73), showed more coarse clean sand grains ~ 1 mm in size on the crest of ripples inside the dust devil track than outside of it. Outside of the track, MI observations showed sand grains set in a matrix of finer grains, inferred to be dust (Greeley et al., 2004 ; Greeley et al., 2006). The present photometric results support the idea that dust devils, and more generally wind effects, are able to remove dust and fine grains, leaving behind low albedo units revealing a dark basaltic substrate comprising coarse-grained materials.

Given the overall patterns derived from the PCA analysis, it is quite possible that the observed photometric variation at least for the western and central part of the crater is partly driven by the prevailing wind regimes considered to be oriented north-northwest/ south-southeast (Greeley et al., 2006), continuously disturbing (sweeping, abrading, pressing, packing, dust removing) the very upper surface layer. Interestingly, one notes that the mapping aspect of the present investigation appears quite useful to provide a better sense of the meaning of the observed photometric variations. The present results support the idea

raised by several authors (e.g., Shkuratov and Helfenstein, 2001; Cord et al., 2003; Piatek et al., 2004; Shkuratov et al., 2005; Shepard and Helfenstein, 2007) that the photometric meaning provided by the Hapke modeling is not pertinent at the particle level but rather delivers complex information related to the surface organization (surface roughness, packing state, …) involving more than a simple physical characterization of the intrinsic optical properties of the constitutive particles. As already suggested (Johnson et al., 2006), one should consider the local topography in modeling the wind patterns and regimes to address the variability and efficiency of eolian weathering activity across Gusev (see Fig. 22 in Greeley et al., 2006)).

7. Conclusions

Some important results have been reached from this exploratory study demonstrating that one can document from orbit the photometric diversity of the martian surface properties. On the operational viewpoint, both the Minnaert and Hapke photometric modeling implemented here demonstrate that HRSC multi-angular observations acquired during the mission with different orbits can be, under some limitations (trade-off between atmospheric opacity and incidence, emission angles), pieced together to derive integrated phase functions at moderate spatial resolution, on the order of 400 m -1.6 km. Advanced DTM products should permit to work at higher spatial resolution. However, new strategies should be considered for the future instruments (e.g., widening the range of geometry and increasing the number of multi angular measurements for a given orbital observation). Also, as progress is made in the modeling, atmospheric contribution should be subtracted from the integrated atmosphere/surface spectrophotometric signal (Vincendon et al., 2007; Vincendon et al., 2008) so that our approach can be both refined and extended to all HRSC multiangular observations. The present lack of atmospheric correction may result in an overestimation of the amount of

forward scattering intrinsically associated with the surface properties.

On the scientific side, this work reveals that one can document from orbit the photometric diversity of the surface properties. The imaging aspect of HRSC observations and the integrated scale at which the Hapke parameters are derived here contribute to the physical meaning of the outputs produced from the Hapke model. As suggested recently (e.g., Cord et al., 2003 ; Piatek et al., 2004; Shkuratov et al., 2005; Shepard and Helfenstein, 2007), the Hapke model is likely not to be pertinent at the level of the particles in the case of close-packed media such as planetary regoliths, but rather delivers complex information related to the surface organization (surface roughness, packing state, …) involving more than a simple physical characterization of the intrinsic optical properties of the constitutive particles.

The most pronounced photometric changes are observed in the yellow, magenta and green units, associated with the low-albedo features corresponding to dark streaks. These three units have a low single scattering albedo, are the most backscattering surfaces across Gusev and Apollinaris, have a high surface roughness and present variable surface states as shown by the opposition parameters estimates, consistent with the occurrence of large basaltic sand grain sizes organized in more or less packed layers.

It is quite remarkable to note within Gusev Crater the convergence of interpretations relying on independent investigations based on thermal inertia, reflectance spectroscopy, in situ microscopic imaging, in situ photometric studies and the present orbital photometric imaging data. It hints at exploring in great detail the possible interplay between rocks, soils and eolian weathering activity as the photometric variability depicted in this paper may arise from the physical surface processes responsible for the surface texture caused by transport, erosion and deposition, and / or from the in situ geochemical processes of alteration and diagenesis likely to occur in the martian soils and subsurface layers. All of these processes are very likely

related to the interaction of the surface with the martian atmosphere circulation and / or ancient hydrosphere/cryosphere regime (Gregg et al., 2007).

A corollary of the present results is that a cautious approach should be taken in addressing the detection of martian variable features based on qualitative inspections of albedo contrasts and brightness variations (Greeley et al., 2007). A more advanced strategy should take advantage of the HRSC multi-angular observations repeated through time under close geometry and illumination conditions in order to separate out true surface changes through time from optical changes induced by the surface photometric properties.

Acknowledgments :

For this study, the HRSC Experiment Team of the German Aerospace Center (DLR) in Berlin has provided map-projected HRSC image data, and HRSC Preliminary 200m DTM(s). We thank the HRSC Experiment teams at DLR Berlin and the Freie Universität Berlin as well as the Mars Express Project Teams at ESTEC (with a special mention for Augustin Chicarro as the Mars Express's Project scientist) and ESOC for the planning and acquisition of data, and for making the processed data available to the HRSC team. We also acknowledge the support of the Co-investigator Team which has contributed in scientific discussions. The research was supported by the French Space Agency CNES and PNP (Programme National de Planétologie) and has benefited from the scientific environment of Paul Sabatier University (Toulouse). We are very grateful to Jeff Johnson and Jason Soderblom for their valuable reviews and careful reading which helped improving this paper.

References :

Adams, J. B., Smith, M.O., and Johnson, P.E. 1986. Spectral mixture modeling : A new analysis of rock and soil types at the Viking Lander site. J.G.R. 91, 8098-8112.

Adams, J. B., and A. R. Gillespie , 2006. Remote Sensing of Landscapes with Spectral Images: A Physical Modeling Approach. Cambridge Univ. Press, 362 pp., New York.

Arvidson, R.E. Guinness , E.A., and Zent, A.P., 1982. Classification of surface units in the equatorial region of Mars based on Viking Orbiter color, albedo, and thermal data. J.G.R. 87, 10149-10157.

Arvidson, R.E., E.A. Guinness, M.A. Dale-Bannister, J. Adams, M. Smith, P.R. Christensen, and R.B. Singer, 1989. Nature and distribution of surficial deposits in Chryse Planitia and vicinity, Mars. J. Geophys. Res., 94, 1573-1587.

Arvidson, R. E., et al. 2004. Localization and physical properties experiments conducted by Spirit at Gusev Crater. Science 305, 821–824.

Arvidson, R. E., et al., 2006, Overview of the Spirit Mars Exploration Rover Mission to Gusev Crater: Landing site to Backstay Rock in the Columbia Hills. J. Geophys. Res., 111, E02S01, doi:10.1029/ 2005JE002499.

Baratoux, D., P. C. Pinet, V. G. Kaydash1,Y. Shkuratov, Y. Daydou, S. Besse, A. Jehl, S. Chevrel, 2006. The derivation of Hapke parameters using multi-angular observations from orbit and laboratory: an ill-posed inverse problem. Lunar Planet. Sci. 37th, Abstract #1340.

Bell, J.F., III, M.J. Wolff, T.C. Daley, D. Crisp, P.B. James, S.W. Lee, J.T. Trauger, and R.W. Evans, 1999. Near-infrared imaging of Mars from HST: Surface reflectance, photometric properties, and implications for MOLA data. Icarus 138, 25-35.

Bell, J. F., III, et al., 2004. Pancam multispectral imaging results from the Spirit rover at Gusev Crater. Science 305(5685), 800– 806, doi:10.1126/ science.1100175.

Chevrel, S. D., Pinet, P. C., Daydou, Y., Maurice, S., Lawrence, D. J., Feldman, W. C., Lucey, P. G., 2002. Integration of the Clementine UV-VIS spectral reflectance data and the Lunar Prospector gamma-ray spectrometer data: A global-scale multielement analysis of the lunar surface using iron, titanium, and thorium abundances. JGR-Planets, 107(E12), 5132.

Christensen, P.R., S.W. Ruff, R. Fergason, N. Gorelick , B.M. Jakosky, M.D. Lane, A.S. McEwen , H.Y. McSween , G.L. Mehall , K. Milam, J.E. Moersch, S.M. Pelkey, A.D. Rogers, M.B. Wyatt, 2005. Mars Exploration Rover candidate landing sites as viewed by THEMIS. Icarus 176, 12–43.

Clancy, R. T. and S. W. Lee, 1991. A new look at dust and clouds in the Mars atmosphere: analysis of emission-phase-function sequences from global Viking IRTM observations. Icarus 93, 135-158, doi:10.1016/0019-1035(91)90169-T

Clancy, R. T., M. J. Wolff, and P. R. Christensen, 2003. Mars aerosol studies with the MGS TES emission phase function observations: Optical depths, particle sizes, and ice cloud types versus latitude and solar longitude. J. Geophys. Res., 108(E9), 5098, doi : 10.1029 / 2003JE002058

Clark, B.E., Helfenstein, P., Bell III, J.F., Veverka, J., Izenberg, N.I., Domingue, D., Wellnitz, D., McFadden, L.A., 2002. NEAR infrared spectrometer photometry of Asteroid 433 Eros. Icarus 155, 189–204.

Combes, M. and 19 authors, 1991. Martian atmosphere studies from the ISM experiment. Planet. Space Sci. 39, 189-198.

Cord, A., P.C. Pinet, Y. Daydou, and S. Chevrel, 2003. Planetary regolith surface analogs : optimized determination of Hapke parameters using multi-angular spectro-imaging laboratory facility. Icarus 165, 414 - 427.

Cord, A., P.C. Pinet, Y. Daydou, and S. Chevrel, 2005. Experimental determination of the

surface photometric contribution in the spectral reflectance deconvolution processes for a simulated martian crater-like regolithic target. Icarus 175, 1, 78-91.

Cord, A., Baratoux, D., Mangold, N., Martin, P., Pinet, P., Greeley, R., Costard, F., Masson, P., Foing, B., Neukum, G. and HRSC team, 2007. Surface roughness and geological mapping at sub-hectometer scale from the HRSC camera onboard Mars Express. Icarus 191, doi:10.1016/j.icarus.2007.04.029.

de Grenier M. and P.C. Pinet, 1995. Near-opposition martian limb darkening: Quantification and implication for visible-near-infrared bidirectional reflectance studies, Icarus 115, 354-368.

Drossart, P., J. Rosenqvist, S. Erard, Y. Langevin, J.P. Bibring, and M. Combes 1991. Martian aerosols properties from the Phobos/ISM experiment. Ann. Geophys. 9, 754-760.

Erard, S., J.F. Mustard, S. Murchie, J.P. Bibring, P. Cerroni, and A. Coradini, 1994. Martian aerosols : near-infrared spectral properties and effects on the observation of the surface. Icarus 111, 313-337.

Esposito, F., M. Giuranna , A. Maturilli , E. Palomba , L. Colangeli , V. Formisano , 2007. Albedo and photometric study of Mars with the Planetary Fourier Spectrometer on-board the Mars Express mission. Icarus 186, 527–546, doi:10.1016/j.icarus.2006.08.028

Farrand, W. H., J. F. Bell III, J. R. Johnson, S. W. Squyres, J. Soderblom, and D. W. Ming, 2006. Spectral variability among rocks in visible and near-infrared multispectral Pancam data collected at Gusev Crater: Examinations using spectral mixture analysis and related techniques. J. Geophys. Res., 111, E02S15, doi:10.1029/2005JE002495.

Foley, D.J., P.L. Whelley, R. Greeley, L.D.V. Neakrase, 2005. Dust Devil Tracks on Mars : Observation and Analysis from Orbit and the Surface, Lunar Planet. Sci. 36th, Abstract # 1162.

Fischer, E. and C.M., Pieters, 1993. The continuum slope of Mars : Bidirectional reflectance

investigations and applications to Olympus Mons, Icarus 102, 185-202.

Geissler, P. E. and Singer, R. B. 1992. Spectrophotometric Mapping of Coprates Quadrangle, Mars. Lunar and Planetary Institute Conference Abstracts 23, 403.

Greeley, R., S. W. Squyres, R. E. Arvidson, P. Bartlett, J. F. Bell III, D. Blaney, N. A. Cabrol, J. Farmer, B. Farrand, M. P. Golombek, S. P. Gorevan, J. A. Grant, A. F. C. Haldemann, K. E. Herkenhoff, J. Johnson, G. Landis, M. B. Madsen, S. M. McLennan, J. Moersch J. W. Rice Jr., L. Richter, S. Ruff, R. J. Sullivan, S. D. Thompson, A. Wang, C. M. Weitz, P. Whelley, Athena Science Team, 2004. Wind-related processes detected by the Spirit Rover at Gusev Crater, Mars. Science 305, 810–821.

Greeley, R., B.H. Foing, G. Neukum, P.C. Pinet, M. Van Kan, S.C. Werner, D. Williams, T. E. Zegers and the Mars-Express/HRSC Co-Investigator Science Team, 2005. Fluid lava flows in Gusev Crater, Mars. Journal of Geophysical Research 110 (E5), E05008, doi : 10.1029/2005JE002401.

Greeley, R., R. E. Arvidson, P. W. Barlett, D. Blaney, N. A. Cabrol, P. R. Christensen, R. L. Fergason, M. P. Golombek, G. A. Landis, M. T. Lemmon, S. M. McLennan, J. N. Maki, T. Michaels, J. E. Moersch, L. D. V. Neakrase, S. C. R. Rafkin, L. Richter, S. W. Squyres, P. A. de Souza Jr., R. J. Sullivan, S. D. Thompson, and P. L. Whelley , 2006. Gusev Crater: Wind-related features and processes observed by the Mars Exploration Rover Spirit, J. Geophys. Res., 111, E02S09, doi:10.1029/2005JE002491.

Greeley, R., P. C. Pinet, D. A. Williams, C. Butler-Freeman, L. D. V. Neakrase, and G. Neukum, 2007. Detection of martian variable features as a function of image filter: HRSC Comparisons. Lunar Planet. Sci. 38th, Abstract #1376.

Gregg, T. K. P., J. P. Briner, K. N. Paris, 2007. Ice-rich terrain in Gusev crater, Mars ? Icarus 192, 348–360.

Guinness, E.A., R.E. Arvidson, and I.H.D. Clark, and M.K. Shepard, 1997. Optical scattering

properties of terrestrial varnished basalts compared with rocks and soils at the Viking Lander sites. J. Geophys. Res., 102, 28687-28703.

Gwinner, K., F. Scholten, B. Giese, J. Oberst, R. Jaumann, M. Spiegel, R. Schmidt, G. Neukum, and das HRSC Co-Investigator Team, 2005. Hochauflösende Digitale Geländemodelle auf der Grundlage von Mars Express HRSC-Daten, Photogrammetri e - Fernerkundung-Geoinformation (PFG), 5, 387-394.

Gwinner, K., Scholten, F., Spiegel, M., Schmidt, R., Giese, B., Oberst, J., Jaumann, R., Heipke, C. , Neukum, G., The HRSC Co-Investigator Team. Derivation and validation of high-resolution digital terrain models from Mars-Express HRSC-data, Photogramm. Eng. Remote Sens., in review.

Hapke, B., 1981. Bidirectional reflectance spectroscopy I. Theory. J. Geophys. Res. 86, 3039–3054.

Hapke, B., 1984. Bidirectional reflectance spectroscopy III. Correction for macroscopic roughness. Icarus 59, 41–59.

Hapke, B., 1986. Bidirectional reflectance spectroscopy IV. The extinction coefficient and the opposition effect. Icarus 67, 264–281.

Hapke, B., 1993. Theory of Reflectance and Emittance Spectroscopy. Cambridge Univ. Press, Cambridge.

Hapke, B., 1999. Scattering and diffraction of light by particles in planetary regoliths. J. Quant. Spectrosc. Radiat. Transfer 61, 565–581.

Hapke, B., 2002. Bidirectional reflectance spectroscopy. 5. The coherent backscatter opposition effect and anisotropic scattering. Icarus 157, 523–534.

Heipke, C., J. Oberst, J. Albertz, M. Attwenger, P. Dorninger, E. Dorrer, M. Ewe, S. Gehrke, K. Gwinner, H. Hirschmüller, J. R. Kim, R. L.Kirk, H. Mayer, J.-P. Muller, R. Rengarajan,

M. Rentsch, R. Schmidt, F.Scholten, J. Shan, M. Spiegel, M. Wählisch, G. Neukum, HRSCCo-Investigator Team, 2007: Evaluating planetary digital terrain models-- The HRSC DTM test, Planetary and Space Science, in press.

Helfenstein, P. and J. Veverka, Photometric properties of lunar terrains derived from Hapke's equation. Icarus, 72, 342-357, 1987.

Helfenstein, P., Veverka, J., Thomas, P.C., Simonelli, D.P., Klaasen, K., Johnson, T.V., Fanale, F., Granahan, J., McEwen, A.S., Belton, M., Chapman, C.R., 1996. Galileo photometry of Asteroid 243 Ida. Icarus 120, 48–65.

Helfenstein, P., Shepard, M., 1999. Submillimeter-scale topography of the lunar regolith. Icarus 141, 107–131.

Herkenhoff, K.E., S. W. Squyres, R. Arvidson, D. S. Bass, J. F. Bell III, P. Bertelsen, N. A. Cabrol, L. Gaddis, A. G. Hayes, S. F. Hviid, J. R. Johnson, K. M. Kinch, M. B. Madsen, J. N. Maki, S. M. McLennan, H. Y. McSween, J. W. Rice Jr., M. Sims, P. H. Smith, L. A. Soderblom, N. Spanovich, R. Sullivan, A. Wang, 2004. Textures of the Soils and Rocks at Gusev Crater from Spirit's Microscopic Imager. Science 305, 824-826, doi :10.1126/science.3050824.

Jakosky, B. M., B. M. Hynek, S. M. Pelkey, M. T. Mellon, S. Martínez-Alonso, N. E. Putzig, N. Murphy, P. R. Christensen, 2006. Thermophysical properties of the MER and Beagle II landing site regions on Mars. J. Geophys. Res., 111, E08008, doi:10.1029/2004JE002320.

Jaumann, R., G. Neukum, T. Behnke, T.C. Duxbury, K. Eichentopf, J. Flohrer, S.v. Gasselt, B. Giese, K. Gwinner, E. Hauber, H. Hoffmann, A. Hoffmeister, U. Köhler, K.-D. Matz, T.B. McCord, V. Mertens, J. Oberst, R. Pischel, D. Reiss, E. Ress, T. Roatsch, P. Saiger, F. Sc holten, G. Schwarz, K. Stephan, M. Wählisch, and the HRSC Co-Investigator Team, 2007. The high-resolution stereo camera (HRSC) experiment on Mars Express: Instrument aspects

and experiment conduct from interplanetary cruise through the nominal mission, Planetary and Space Science, 55, 928-952.

Jehl, A., 16 authors and The Co-I Mars-Express HRSC team, 2006. Improved surface photometric mapping across Gusev and Apollinaris from an HRSC/Mars Express integrated multi-orbit dataset : implication on Hapke parameters determination. Lunar Planet. Sci. 37th, # 1219.

Johnson, J. R., R. Kirk, L. A. Soderblom, L. Gaddis, R.J. Reid, D.T. Britt, P. Smith, M. Lemmon, N. Thomas, J.F. Bell III, N.T. Bridges, R. Anderson, K.E. Herkenhoff, J. Maki, S. Murchie, A. Dummel, R. Jaumann, F. Trauthan, G. Arnold, Preliminary results on photometric properties of materials at the Sagan Memorial Station, Mars, *J. Geophys. Res.,* 104, 8809-8830, 1999.

Johnson, J.R., W.M. Grundy, M.T. Lemmon, J.F. Bell III, M.J. Johnson, R. Deen, R.E. Arvidson, W. Farrand, E. Guinness, K.E. Herkenhoff, F. Seelos IV, J. Soderblom, and S. Squyres, Spectrophotometric properties of materials observed by Pancam on the Mars Exploration Rovers: 1. Spirit, 2006. J. Geophys. Res., 111, E02S14, doi:10.1029/2005JE002494.

Johnson, J. R. ,J. F. Bell III, P. Geissler, W. M. Grundy, E. A. Guinness, P. C. Pinet, J. Soderblom, Physical properties of the martian surface from spectrophotometric observations, Ch. 19, in The Martian Surface : Composition, Mineralogy, and Physical Properties, in press, Cambridge university Press, 2008.

Kaydash, V.G., P. C. Pinet, D. Baratoux, S. Besse, A. Jehl, S. Chevrel, 2006. Lunar photometry from Clementine multiangular data: analysis of Hapke parameters estimate and implication for upcoming Smart-1 spot-pointing data. Lunar Planet. Sci. 37th, Abstract #1340.

Kieffer, H.H., T.Z. martin, A.R., Peterfreund, B.M., Jakovsky, E.D., Miner, and F.D., Palluconi 1977. Thermal and albedo mapping of Mars during the Viking primary mission. J.G.R. 82, 4249-4291.

Kreslavsky, M.A., N. V. Bondarenko, P. C. Pinet, J. Raitala, G. Neukum and The Mars Express HRSC Co-Investigator Team, 2006. Mapping of photometric anomalies of martian surface with HRSC data. Lunar Planet. Sci. 37th, Abstract # 2211.

Lemmon, M. T., et al. (2004), Atmospheric imaging results from the Mars Exploration Rovers: Spirit and Opportunity, Science, 306, 1753-1756, doi:10.1126/science.1104474.

Lemmon, M. T., and the Athena Science Team, 2006, Mars Exploration Rover atmospheric imaging: dust storms, dust devils, dust everywhere, Lunar Planet. Sci. 37th.

Lichtenberg, K. A. , R. E. Arvidson, F. Poulet, R. V. Morris, A. Knudson, J. F. Bell, G. Bellucci, J.-P. Bibring, W. H. Farrand, J. R. Johnson, D. W. Ming, P. C. Pinet, A. D. Rogers, S. W. Squyres, 2007. Coordinated Analyses of Orbital and Spirit Rover Data to Characterize Surface Materials on the Cratered Plains of Gusev Crater, Mars. J. Geophys. Res., 112, E12S90, doi:10.1029/2006JE002850.

Lohse V., Heipke C., Kirk R.L., 2006. Derivation of planetary topography using multi-image shape-from-shading. Planetary and Space Science, Vol. 54, No. 7, 661-674.

Martin P., Pinet P.C., Bacon R., Rousset A., Bellagh F., martian surface mineralogy from 0.8-1.05 μm TIGER spectro-imagery measurements in Terra Sirenum and Tharsis Montes Formation, 1996. Planetary and Space Science 44, (8), 859-888.

Martınez-Alonso, S., B. M. Jakosky, M. T. Mellon, and N. E. Putzig, 2005. A volcanic interpretation of Gusev Crater surface materials from thermophysical, spectral, and morphological evidence. J. Geophys. Res., 110, E01003, doi:10.1029/2004JE002327.

McCord, T.B., J. B. Adams, G. Bellucci, J-P. Combe, A. R. Gillespie, G. Hansen, H. Hoffmann, R. Jaumann, G. Neukum, P.C. Pinet, F. Poulet, K. Stephan, the HRSC

Spectrophotometric Working group, and the HRSC Co-I Team, 2007. The Mars Express High Resolution Stereo Camera Spectrophotometric Data: Characteristics and Science Analysis. Journal of Geophysical Research (Planets), 112, E06004, doi:10.1029/2006JE002769

McEwen, A.S., 1991. Photometric functions for photoclinometry and other applications. Icarus 92, 298–311.

Milam, K. A., K. R. Stockstill, J. E. Moersch, H. Y. McSween Jr., L. L. Tornabene, A. Ghosh, M. B. Wyatt, and P. R. Christensen, 2003. THEMIS characterization of the MER Gusev Crater landing site. J. Geophys. Res., 108(E12), 8078, doi:10.1029/2002JE002023.

Minnaert, M., 1941. The reciprocity principle in lunar photometry. *Astrophys. J.* 93, 403-410.

Murchie, S.L., Mustard, J.F., Bishop, J.L., Head, J.W., Pieters, C.M. and Erard, S. 1993. Spatial variations in the spectral properties of bright regions of Mars. Icarus 105, 454-468.

Mushkin, A., and A. R. Gillespie, 2005. Estimating sub-pixel surface roughness using remotely sensed stereoscopic data. Remote Sens. Environ. 99, 75– 83.

Mushkin, A., and A. R. Gillespie, 2006. Mapping sub-pixel surface roughness on Mars using high-resolution satellite image data. Geophys. Res. Lett. 33(18), L18204, doi:10.1029/2006GL027095.

Mustard, J.F. and J.F. Bell, 1994. New composite reflectance spectra of Mars from 0.4 to 3.14 micron. G.R.L. 21 (5), 353-356.

Pinet, P.C. and S.D., Chevrel, JGR 1990. Spectral identification of geological units on the surface of Mars related to the presence of silicates from earthbased near-infrared telescopic CCD imaging. Journ. Geoph. Res. (Mars special issue) 95 (B9), 14435-14446.

Pinet P C., Shevchenko V.V., Chevrel S.D., Daydou Y.H. Rosemberg C., Local and regional

lunar regolith characteristics at Reiner Gamma formation : Optical and spectroscopic properties from Clementine and Earth-based data, 2000. J. Geophys. Res. 105 (E4), 9457-9475.

Pinet, P. C., A. Cord, Y. Daydou, F. Boubault, S. Chevrel, and V. Lapeyrere, 2001. Influence of linear versus non-linear mixture on bidirectional reflectance spectra using a laboratory wide field spectral imaging facility. Lunar Planet. Sci 32nd. Abstract #1552.

Pinet, P. C. and C. Rosemberg, 2001. Regional Photometry and Spectral Albedo of the Eastern Hemisphere of Mars in the 0.7 – 1 micron domain. Lunar Planet. Sci. 32nd, Abstract #1640.

Pinet, P. C., A. M. Cord, S. Chevrel, and Y. Daydou, 2004. Optical response and surface physical properties of the lunar regolith at Reiner Gamma formation from Clementine orbital photometry: derivation of the Hapke parameters at local scale. Lunar Planet. Sci. 35th. Abstract # 1660.

Pinet, P.C., Y. Daydou, A. Cord, S.C. Chevrel, F. Poulet, S. Erard, J.P. Bibring, Y. Langevin, R. Melchiorri, Bellucci G., F. Altieri, R.E. Arvidson, and the OMEGA Co-Investigator Team, 2005. Derivation of Mars Surface Scattering Properties from OMEGA Spot Pointing Observations. Lunar Planet. Sci. 36th, #1694.

Pinet, P.C., 18 co-authors and the Mars-Express @ MER Science teams, 2006. Mars Express /HRSC Imaging photometry and MER Spirit / PANCAM in situ spectrophotometry within Gusev. Lunar Planet. Sci. 37th, # 1220.

Poulet, F., J. N. Cuzzi, D. P. Cruikshank, T. Roush, and C. M. Dalle Ore, 2002. Comparison between Shkuratov and Hapke scattering theories for solid planetary surfaces. Application to the surface composition of two Centaurs. Icarus 160, 313-324.

Regner, P., Kamp, L., and Neukum, G. 1988. Multispectral Photometric Classification and

Mapping of the martian Surface in the Oxia Palus Region. Lunar and Planetary Institute Conference Abstracts 19, 968.

Scholten, F., Gwinner, K., Roatsch, T., Matz, K.-D., Waehlisch, M., Giese, B., Oberst, J., Jaumann, R., Neukum, G., and the HRSC Co-Investigator Team, 2005. Photogrammetric Engineering & Remote Sensing 71 (10), 1143-1152.

Shepard, M.K., Campbell, B.A., 1998. Shadows on a planetary surface and implications for photometric roughness. Icarus 134, 279–291.

Shepard, M. K., and P. Helfenstein, 2007. A test of the Hapke photometric model. J. Geophys. Res., 112, E03001, doi:10.1029/2005JE002625.

Shkuratov, Yu., Starukhina, L., Hoffman, H., Arnold, G., 1999. A model of spectral albedo of particulate surfaces: implications for optical properties of the moon. Icarus 137, 235–246.

Shkuratov, Yu.G. and P. Helfenstein 2001. The opposition effect and the quasi-fractal structure of regolith: I. Theory. Icarus 152, 96-116.

Shkuratov, Y. G., D. G. Stankevich, D. V.Petrov, P. C. Pinet, A. M. Cord, Y. H. Daydou, S. D. Chevrel. Interpreting photometry of regolith-like surfaces with different topographies: shadowing and multiple scattering. Icarus 173, 3-15, 2005.

Simonelli, D.P., Rossier, Laura, Thomas, P.C., Veverka, J., Burns, J.A., Belton, M.J.S., 2000. Leading/trailing albedo asymmetries of Thebe, Amalthea, and Metis. Icarus 147, 353–365.

Soderblom,,J.M., J. F. Bell III , Min Y.H. Hubbard , M. J. Wolff, 2006. martian phase function: Modeling the visible to near-infrared surface photometric function using HST-WFPC2 data. Icarus 184, 401–423

Spiegel , M., 2007. Improvement of interior and exterior orientation of the three line camera HRSC with a simultaneous adjustment, Stilla U et al (Eds) PIA07. International Archives of

Photogrammetry, Remote Sensing and Spatial Information Sciences, 36 (3/W49B).

Squyres, S.W. et al., 2004. The Spirit Rover's Athena science investigation at Gusev Crater, Mars. Science 305, 794-799, doi :10.1126/science.3050794.

Strickland, E. L. 1989. Surface Photometric Properties and Albedo Changes in the Central Equatorial of Mars. Lunar and Planetary Institute Conference Abstracts 20, 1081.

Tejfel U.G., N.U. Shinyaeva, A.N. Aksenov, and G. Kharitonova, 1992. The experience of the Mars normal albedo and limb darkening coefficient from the observations during 1990 opposition. Proc. L.P.S.C. 23rd, 1417-1418.

Veverka, J. ,J. Goguen, S. Yang, and J. Elliot, 1978. Scattering of light from particulate surfaces. Icarus 34, 406-414.

Vincendon, M., Y. Langevin, F. Poulet, J.-P. Bibring, and B. Gondet, 2007. Recovery of surface reflectance spectra and evaluation of the optical depth of aerosols in the near-IR using a Monte Carlo approach: Application to the OMEGA observations af high-latitude. J. Geophys. Res. 112, EO8S13, doi:10.1029/2006JE002845.

M. Vincendon, Y. Langevin, A. Pommerol, M. J. Wolff, J.-P Bibring, B. Gondet, D. Jouglet, F. Poulet, 2008. Time Variations of low albedo regions of Mars in the OMEGA/Mex dataset, Lunar Planet. Sci. 39th, Abstract # 1931 . .

Warell, J., Limaye, S.S., 2001. Properties of the Hermean regolith: I. Global regolith albedo variation at 200 km scale from multicolor CCD imaging. Planet. Space Sci. 49, 1531–1552.

Warell, J. 2004. Properties of the Hermean regolith: IV. Photometric parameters of Mercury and the Moon contrasted with Hapke modeling, Icarus 167, 271–286.

Tables:

Table 1. Set of HRSC orbits used in this study, with corresponding acquisition time, Ls: Solar Longitude, Subsolar latitude and longitude, and atmospheric opacity estimate τ (from Lemmon et al., 2006) in the visible range.

Table 2. Geometry of observation for each sensor and orbit (nd refers to nadir, s1 and s2 to stereo, p1 and p2 to photometric HRSC channels; number of configurations ranges from 3 to 5, depending on the number of sensors used for a given orbit). "Mean" indicates the average value for the orbital strip over Gusev while "Spirit location" refers to the geometry under which the Spirit landing site is seen by the HRSC sensor (—indicates that the Spirit landing site is not covered by this observation). Deviation to spec. refers to the Deviation from specularity, the angular distance between the surface normal (assuming no topography) and the theoretical surface normal for which specular conditions occur. As an example, h0024.nd and h2271.nd are approaching this situation.

Table 3. Definition of the four main regions of interest (ROIs) considered in the present analysis. Correspondence is provided between the color coding used, the denomination, and the thermophysical characteristics (thermal inertia and albedo) from THEMIS (Milam et al., 2003) and TES data (Martinez-Alonso et al., 2005).

Table 4. HG2- Hapke parameters determination (mean and associated standard deviation corresponding to the 30 best solutions retrieved by the genetic algorithm).

b, c: phase function parameters; $\overline{\theta}$, macroscopic roughness, *w*: single-scattering parameter; B0 and h: opposition parameters, respectively amplitude and width. Scoabs is the absolute

score (rms absolute residuals in reflectance); scorel is the associated relative score (rms relative residuals in %).

Table 5. HG2- Hapke parameters determination considering no opposition effect (B0=h=0) and a restricted phase angle domain to phase angle > 20° (mean and associated standard deviation corresponding to the 30 best solutions retrieved by the genetic algorithm). b, c: phase function parameters; θ, macroscopic roughness, w: single-scattering parameter. Scoabs is the rms absolute residuals in reflectance; scorel is the associated rms relative residuals in %.

Table 6. HG2- Hapke parameters determination for the 7 units defined from the PCA-classification when the opposition effect parameters are set free (mean and associated standard deviation corresponding to each cluster)

Table 7. HG2- Hapke parameters determination for the 7 units defined from the preceding PCA-classification when the opposition effect is neglected, with phase angles larger than 20° (mean and associated standard deviation corresponding to each cluster)

Figure captions:

Figure 1. Context image (background image: MOC Wide-Angle) with HRSC overlapping frames (color line and number) corresponding to orbit number. Black dotted frame highlights the region where the photometric investigation is carried out. The 4 color dots correspond to selected ROIs located in different thermophysical units (see text).

Figure 2. (2a) Orbit number of HRSC nadir images over Gusev. From top left to bottom right: (top) 24, 72, 637, 648, 987; (bottom) 1879, 2249, 2271, 2685, 2729. Illumination and atmospheric opacity conditions vary with the orbit (see Tables 1 and 2). (2b) 3D renditions for each orbit visualizing the geometries of observation corresponding to the nadir, photometry and stereo HRSC sensors, and the solar illumination condition.

Figure 3. (3a) Elevation and (3b) slope maps from HRSC orbit DTM derived at 400-m resolution. High local slopes are displayed in white. 80% of the surface has a local slope < 5°.

Figure 4. Histogram of the absolute (4a) and relative (4b) residuals determined for each pixel as the rms absolute (relative) standard deviation between Minnaert modeling and HRSC observations with a spatial filtering rejecting pixels with local slope > 3°. Cumulative occurrence is given on the right of the graphs.

Figure 5. Maps of the Minnaert modeling results at 400-m resolution. (5a): Relative score defined as the rms relative residuals when considering 10 to 15 geometric configurations and typically ranging around 5 - 6% (see text). (5b, 5c): Distribution of the k Minnaert coefficient without any spatial filtering (5b) and with a spatial filtering rejecting pixels with local slope> 3° (c). (5d, 5e): Distribution of the Minnaert albedo without any spatial filtering (5d) and with a spatial filtering rejecting pixels with local slope > 3° (5e).

Figure 6. Graph of the k Minnaert exponent as a function of the Minnaert albedo for the pixels with a local slope < 3%. The values corresponding to the 4 selected ROIs (see text, Figure 1 and Table 3) are overlain with symbols: cross for red, star for cyan, diamond for

green, square for yellow.

Figure 7. Maps of the Minnaert modeling results at 100-m resolution around Spirit landing site (location given by the cross). (7a): k distribution; (7b): Minnaert albedo distribution; (7c) relative residuals distribution showing the local residuals increase at the periphery of the dark streak region consistent with the occurrence of local surface changes during the 2-year period of observation.

Figure 8. Location of the 10 selected ROIs (red, green, blue, yellow, cyan, magenta, orange, purple, orchid, chartreuse) used for testing the implementation of Hapke (HG2) modeling on HRSC observations.

Figure 9. Examples of HRSC geometric configurations documenting the phase function with various backward and forward scattering situations, close or far from the principal plane, for a few selected ROIs (Red (a), Green (b), Cyan (c), Yellow (d)) (see also Table 2 'Spirit location'). Incidence i (left), Emergence e (middle) as a function of Azimuth (Az) in polar graphs (i,e: radial distance, Az: polar angle increasing counterclockwise). Retrieved Phase function expressed in reflectance factor (REFF) (right). Asterisk: Orbit 24 (3 observations; Open diamond: Orbit 72 (5 observations); Open upward triangle: Orbit 637 (4 observations); Open square: Orbit 648 (4 observations); X: Orbit 987 (5 observations); Open circle: Orbit 2249 (5 observations); black triangle: Orbit 2271 (5 observations); Cross: Orbit 2685 (3 observations); black circle: Orbit 2729 (3 observations).

Figure 10. Model HG2-Hapke parameters determination, with the opposition parameters set free, for the 10 selected (a) to (j) ROIs (see text). (a) red, (b) green, (c) blue, (d) yellow, (e) cyan, (f) magenta, (g) maroon, (h) purple, (i) orchid, (j) chartreuse.

In each graph, the first 200 best solutions are displayed as a function of the increasing residuals (see text) with b (in black), c (in red): phase function parameters ; $\bar{\theta}$ (in green): macroscopic roughness, *w* (in blue): single-scattering parameter; B0 (in orange) and h (in

pink): opposition parameters, respectively amplitude and width. Vertical scale represents the 0-1 parametric range, with $\bar{\vartheta}$ values divided by 100. The histogram distribution is given for each parameter in its corresponding color, left of the y-axis. The grey color downward histogram at the bottom of each graph represents the distribution of the 200 solutions versus the residuals.

Figure 11: Model HG2-Hapke (b, c) phase function parameters determination, with the opposition parameters set free, for the 10 selected (a) to (j) ROIs (see text). (a) red, (b) green, (c) blue, (d) yellow, (e) cyan, (f) magenta, (g) maroon, (h) purple, (i) orchid, (j) chartreuse. In each graph, the first 30 best solutions are displayed as a function of the increasing residuals (see text) with a color coding ranging from black, blue, green to red.

Figure 12: Model HG2-Hapke macroscopic roughness $\bar{\theta}$ versus single scattering w parameter estimates, with the opposition parameters set free, for the 10 selected (a) to (j) ROIs (see text). (a) red, (b) green, (c) blue, (d) yellow, (e) cyan, (f) magenta, (g) maroon, (h) purple, (i) orchid, (j) chartreuse. In each graph, the first 30 best solutions are displayed as a function of the increasing residuals (see text) with a color coding ranging from black, blue, green to red.

Figure 13: HG2-Hapke (B0, h) opposition parameters determination for the 10 selected (a) to (j) ROIs (see text). (a) red, (b) green, (c) blue, (d) yellow, (e) cyan, (f) magenta, (g) maroon, (h) purple, (i) orchid, (j) chartreuse. In each graph, the first 30 best solutions are displayed as a function of the increasing residuals (see text) with a color coding ranging from black, blue, green to red.

Figure 14. HG2-Hapke modeled phase function (black diamond) versus HRSC observed phase function (orbit symbols as on Fig. 9) expressed in BRDF for the 10 selected (a) to (j) ROIs (see text). (a) red, (b) green, (c) blue, (d) yellow, (e) cyan, (f) magenta, (g) maroon, (h) purple, (i) orchid, (j) chartreuse. BRDF Difference : (observation – model) is displayed below

for each geometric configuration.

Figure 15. Map of the HG2-Hapke (opposition parameters set free) over Gusev Crater and Apollinaris southern flank, with a 1.6x1.6 km2 resolution. (15a) : Distribution of the relative residuals (rms) given in % (see also the corresponding histogram shown on Fig. 16). (15b, c) : Distribution of the phase function parameters b and c. (15d,e) : Distribution of the surface roughness and single scattering albedo parameters $\overline{\theta}$ and *w*. (15f,g) : Distribution of the opposition parameters B0 and h. Based on Fig. 16, areas with relative residuals >8% have been discarded and appear in black on Figs 15b,c,d,e,f,g.

Figure 16. Histogram of the relative residuals (rms) given in % ; one notes a Gaussian distribution centered on 5% with a residual tail beyond 8%.

Figure 17. Distribution of the photometric variations for each Hapke parameter across Gusev Crater and Apollinaris Patera for the population with relative residuals <8% and after the rejection of the anomalous cases presenting a phase function parameter b > 0.9 (see text). b and c phase function parameters; histogram of the mean estimate, with its corresponding standard deviation derived from the 30 best solutions for the b phase function parameter (17a and b), for the c phase function parameter (17c and d), for the θ macroscopic roughness parameter (17e and f), for the *w* single scattering albedo parameter, *w* (17g and h), for the opposition effect parameter, h (17i and j), for the opposition effect parameter, B0 (17k and l). Parameters b, c, *w* present rather low deviations; $\overline{\theta}$ and h parameters present a range of low to intermediate deviations; B0 may present large standard deviations (see text). Dotted lines indicate the cumulative occurrence for the standard deviation histograms.

Figure 18. Photometric classification across Gusev and Apollinaris southern flank from a clustering method based on a principal component analysis (PCA) of the 6 Hapke parameters variations mapped on Fig. 15. Seven units are identified with their distribution displayed on Fig. 18a, and the corresponding clusters in the parametric space shown respectively in the b

versus c phase function graph (Figs. 18b and c (mean and standard deviation of each cluster are displayed with crosses (see also Table 5)), in the $\overline{\theta}$ versus *w* graph (Figs. 18d and e), in the B0 versus h opposition effect graph (Figs. 18f and g)). Corresponding histograms (see Fig. 17) are also plotted in order to give a sense of the density distribution of the data clouds.

Figure 19. Representation of the same photometric clusters produced when considering a phase function truncated below 20° phase angle and thus neglecting the opposition effect (h=B0=0). Figs. 19a and b show the clusters in the b versus c graph and the corresponding mean and standard deviation, displayed with crosses, for each cluster. Same representation in the $\overline{\theta}$ versus *w* graph (Figs. 19c and d). The "orchid" unit is scattered across the parametric space; the same occurs to less an extent to the other clusters and the classification is no longer valid. The opposition effect thus plays a significant role suggesting that the surface optical properties across Gusev are strongly influenced by the porosity and packing characteristics or grain size distribution of the upper layer of the martian regolith.

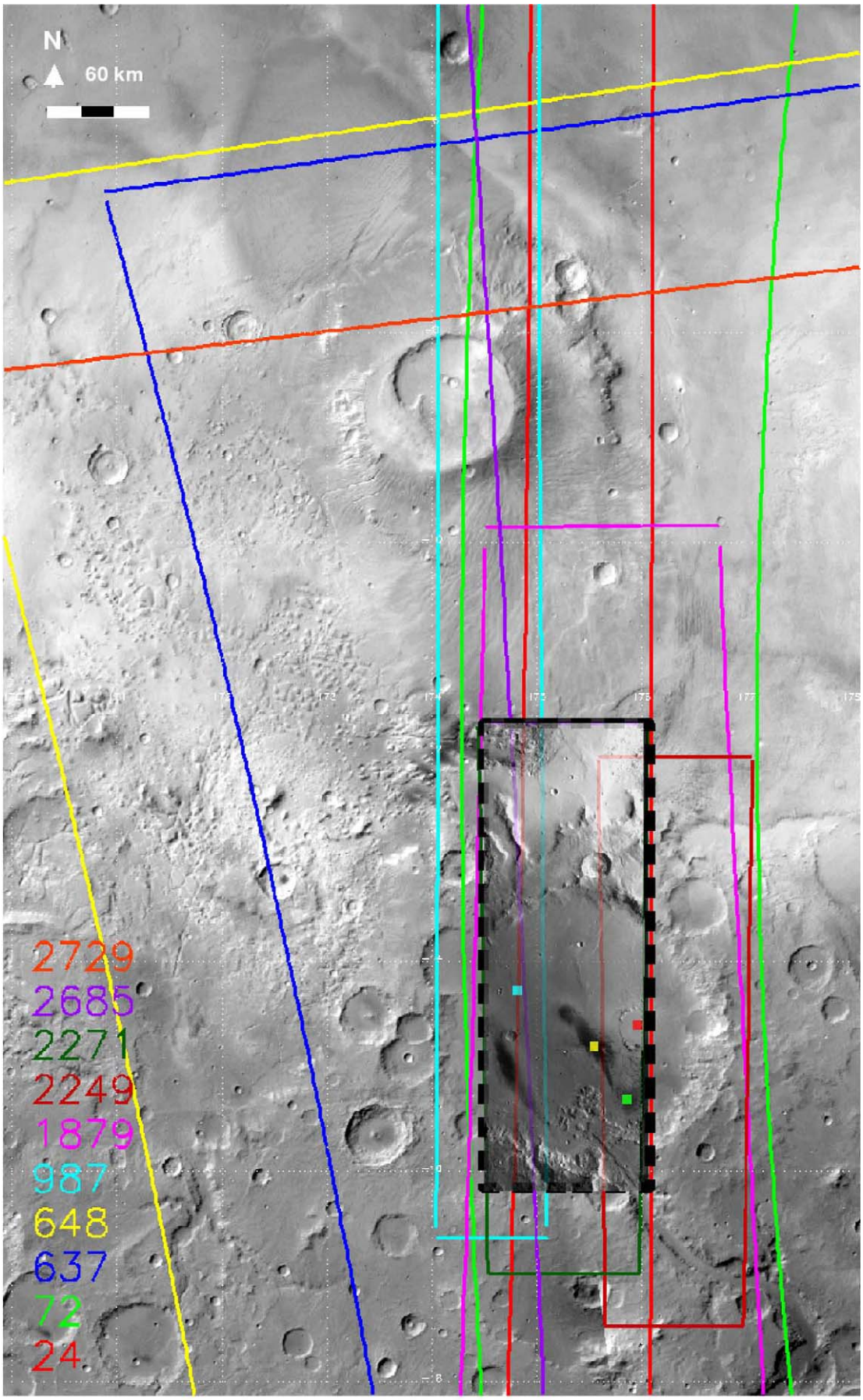

Figure 1:

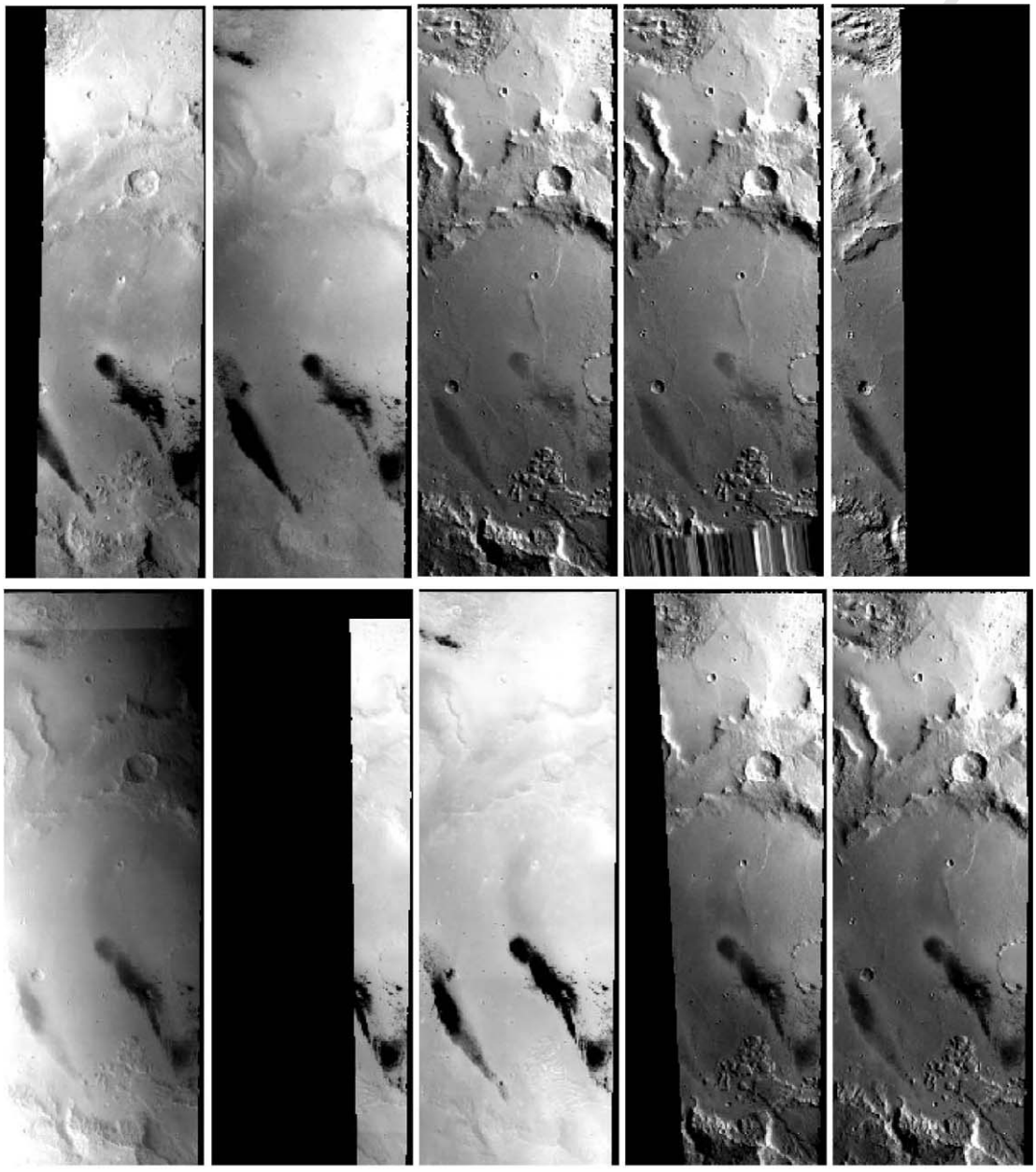

2.a

Figure 2:

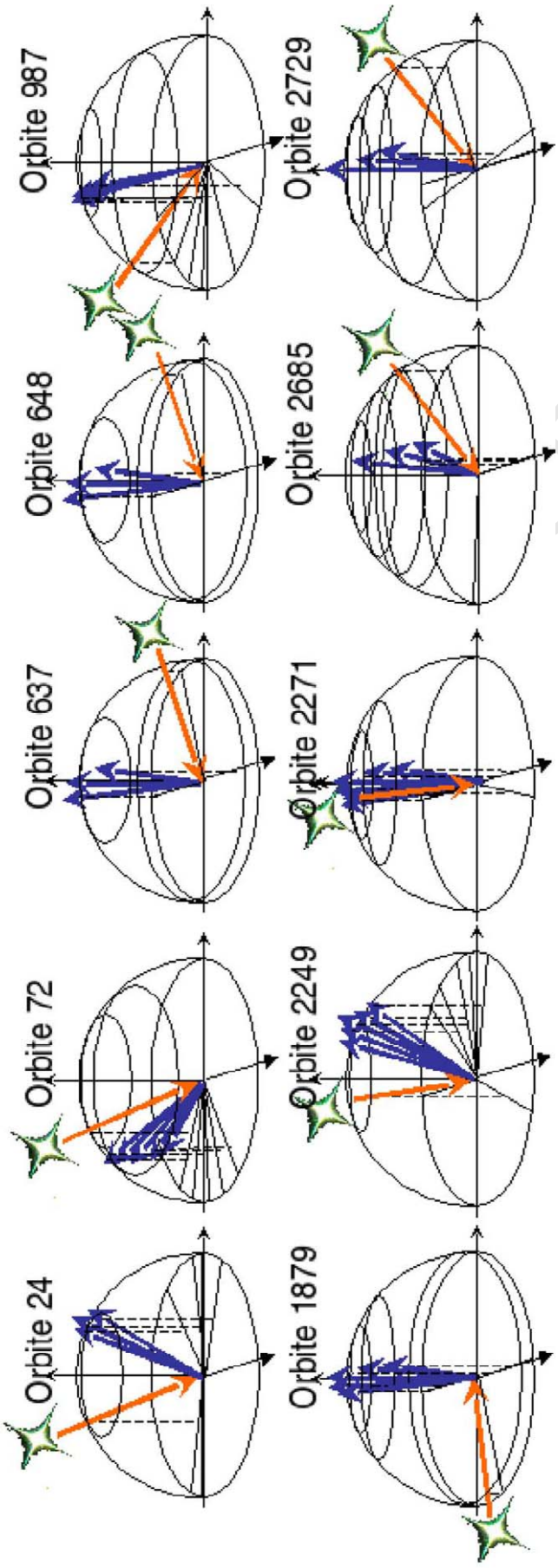

2.b

Figure 2:

I10384_Fig2b

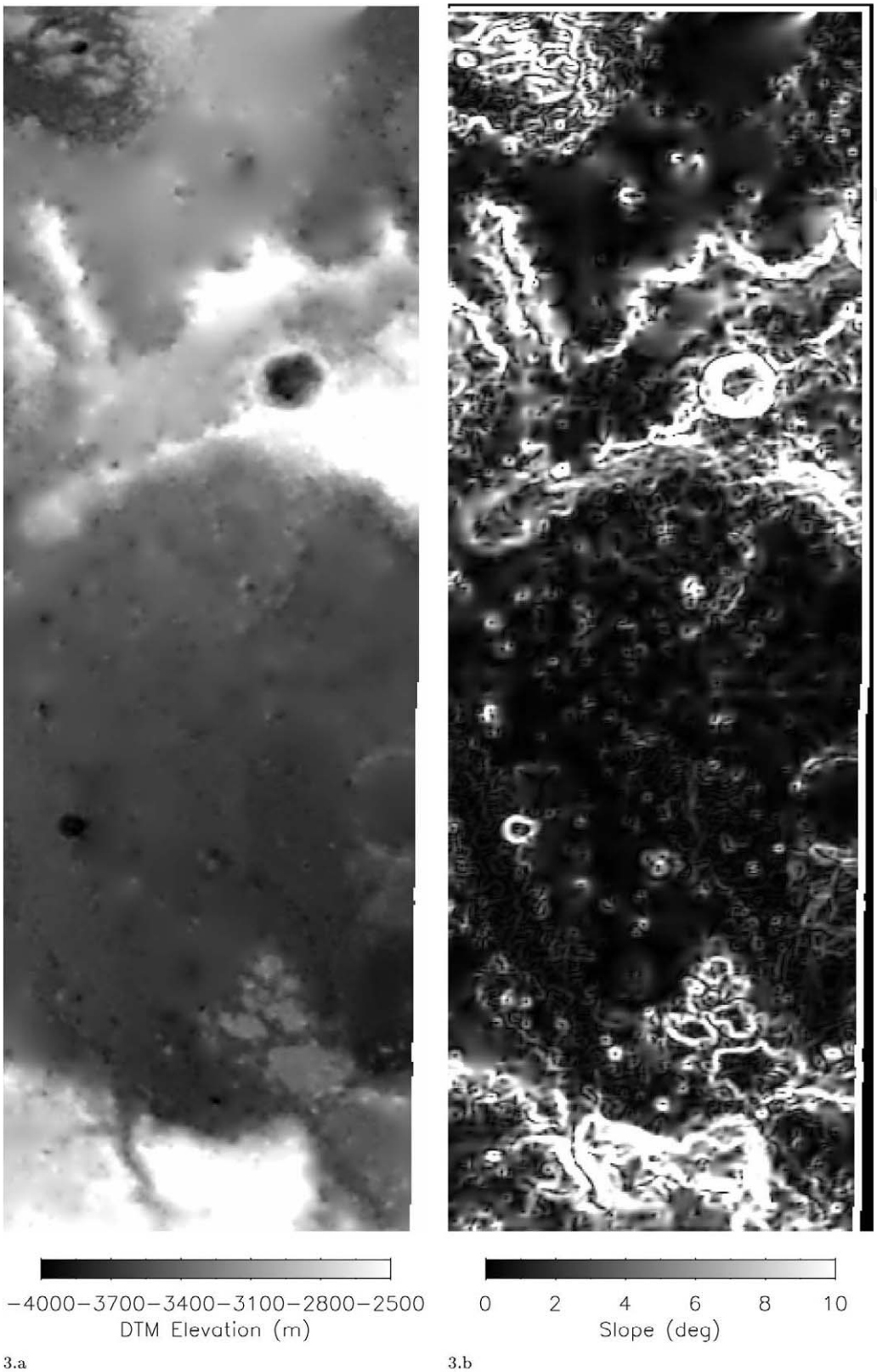

3.a 3.b

Figure 3:

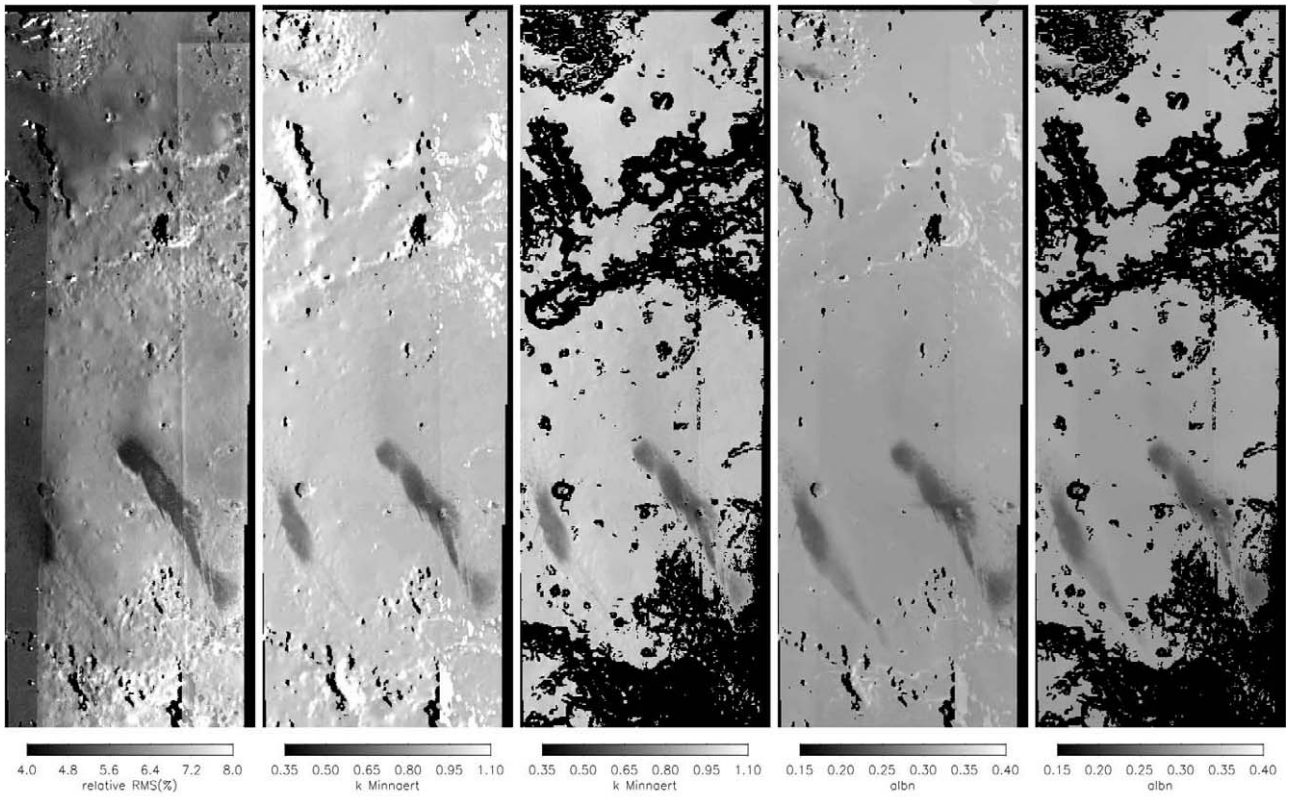

4.a 4.b 4.c 4.d 4.e

Figure 4:

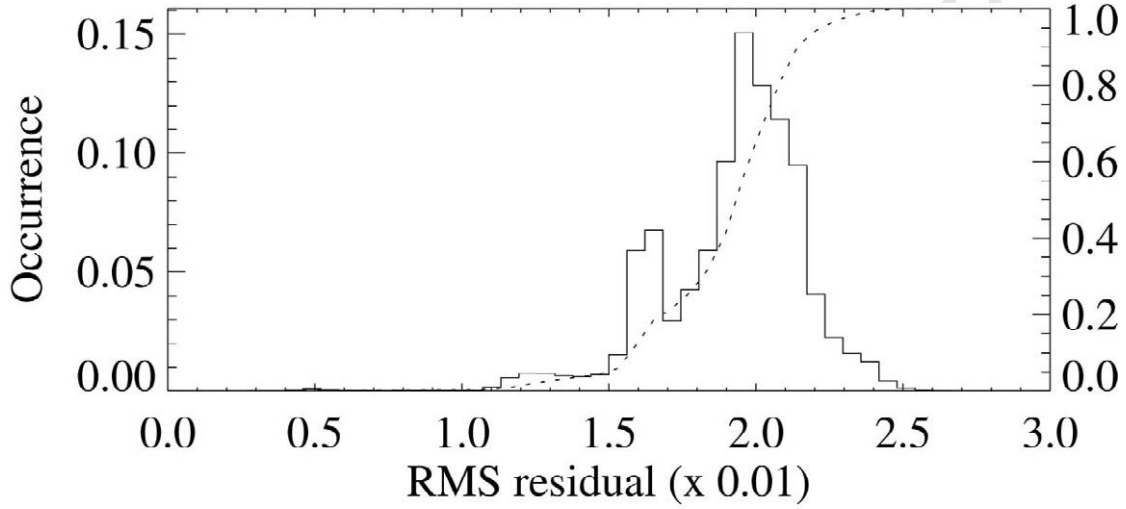

5.a

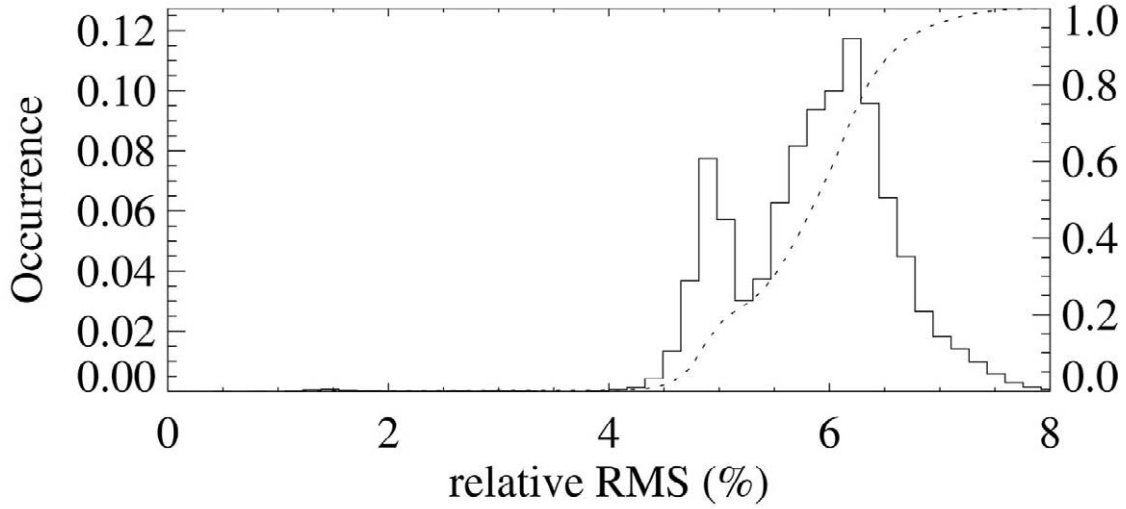

5.b

Figure 5:

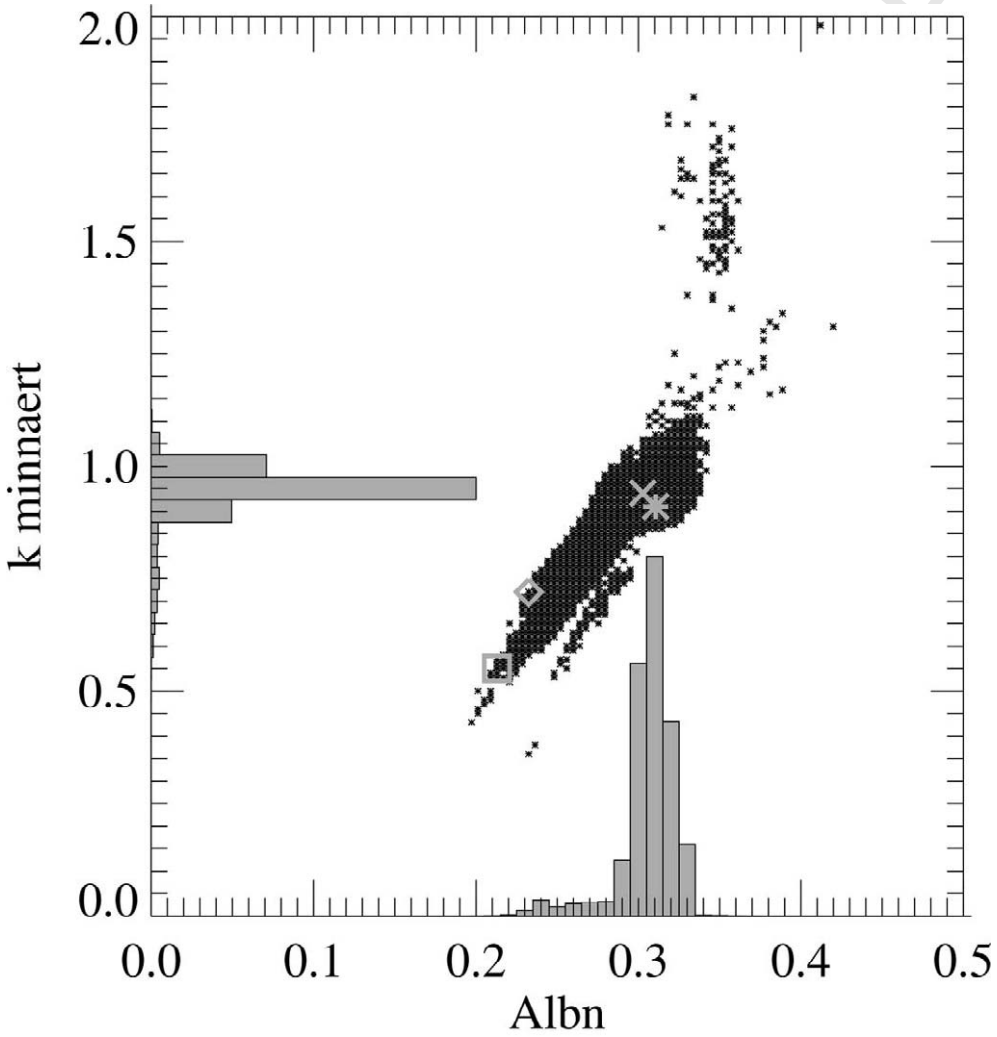

Figure 6:

I10384_Fig6

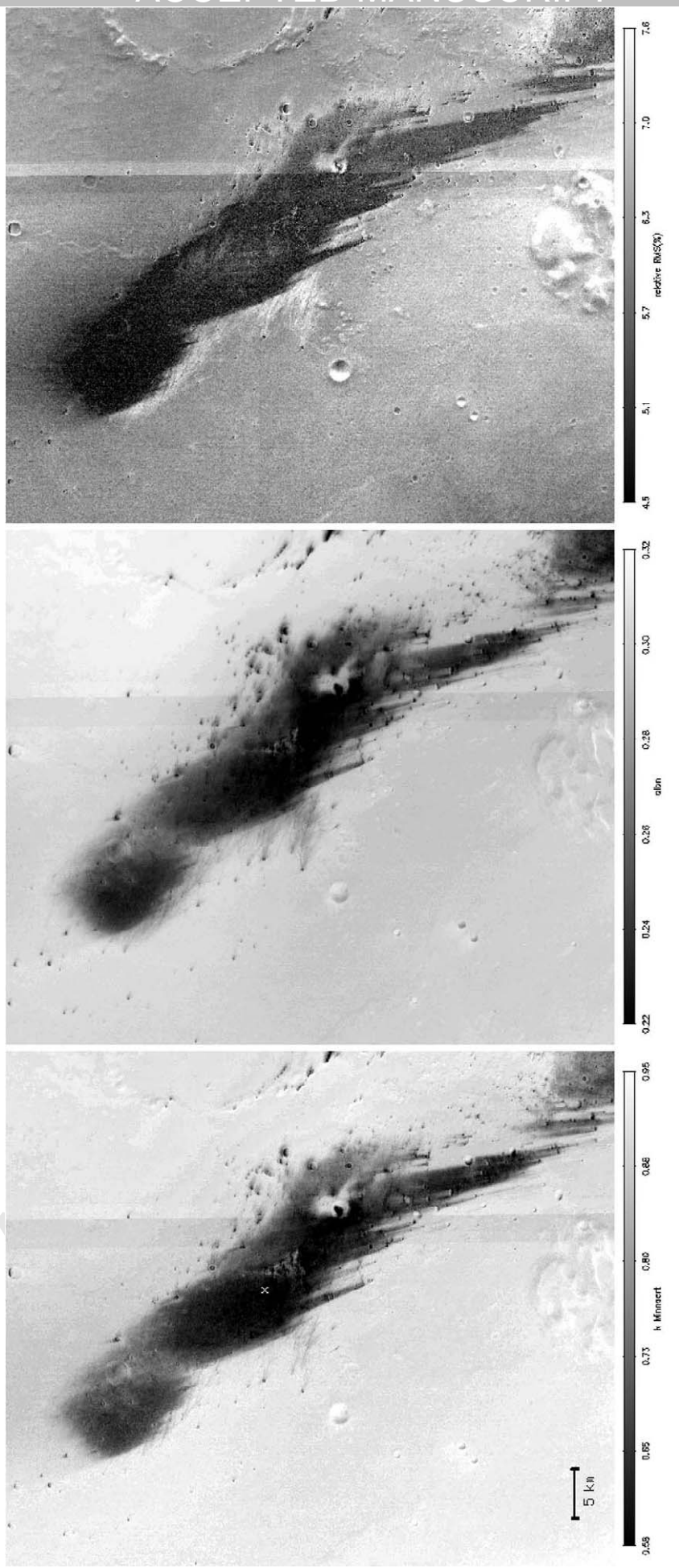

7.a 7.b 7.c

Figure 7:

I10384_Fig7

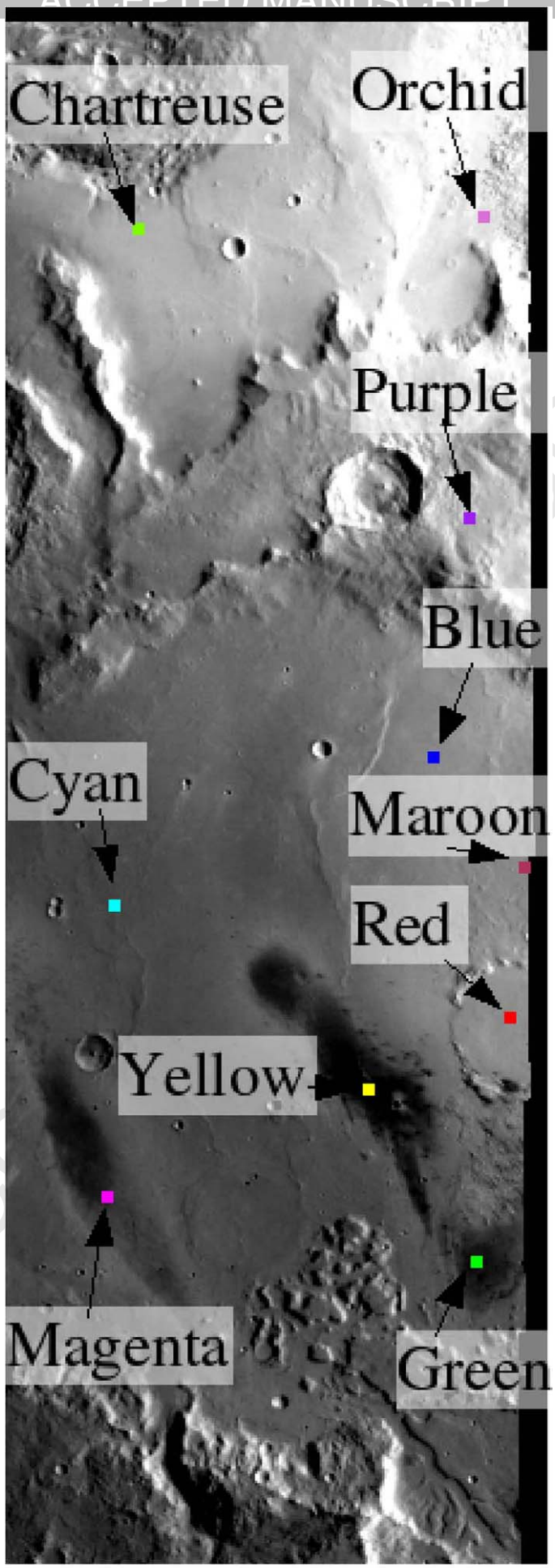

I10384_Fig8

Figure 8:

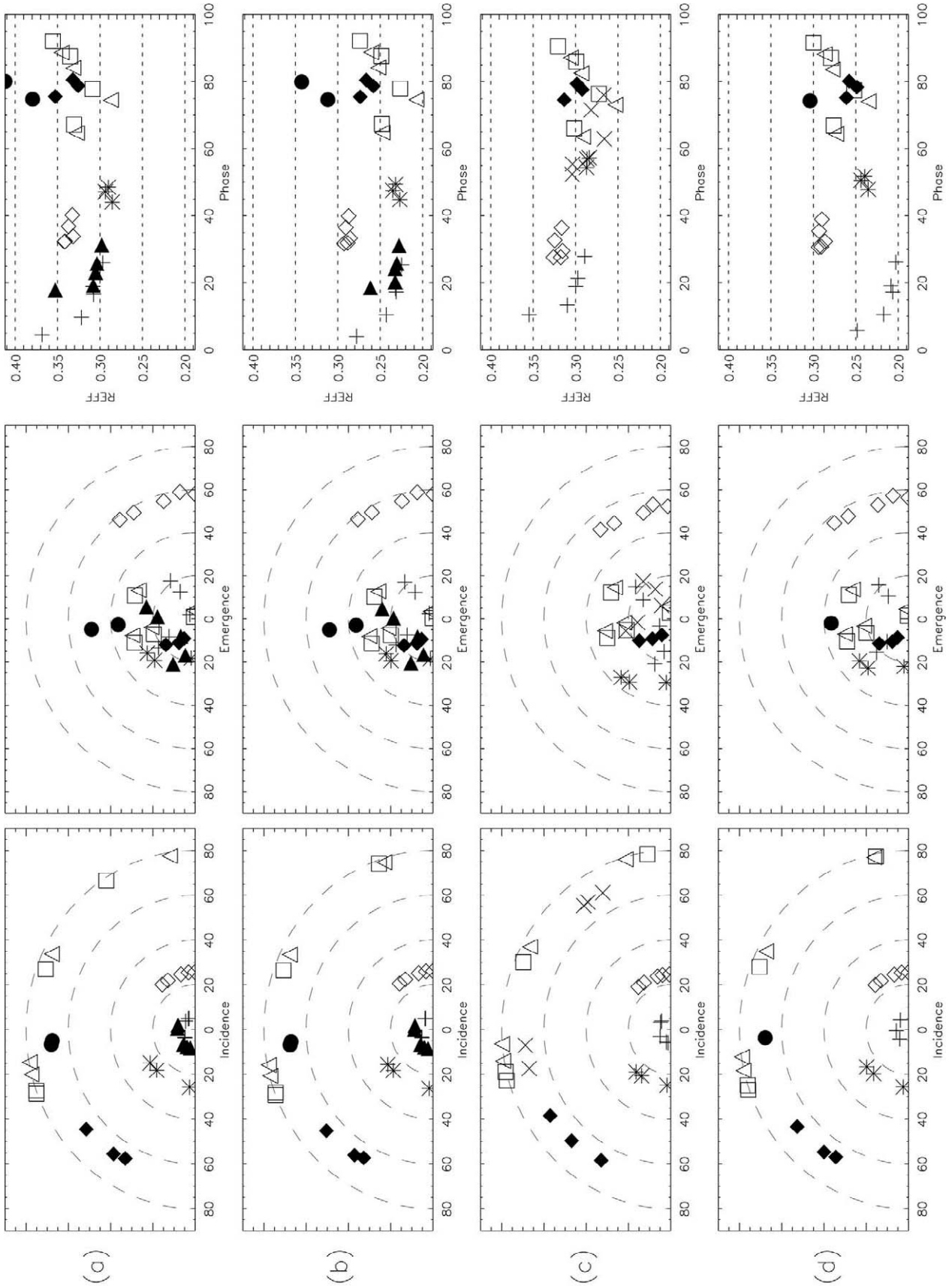

Figure 9:

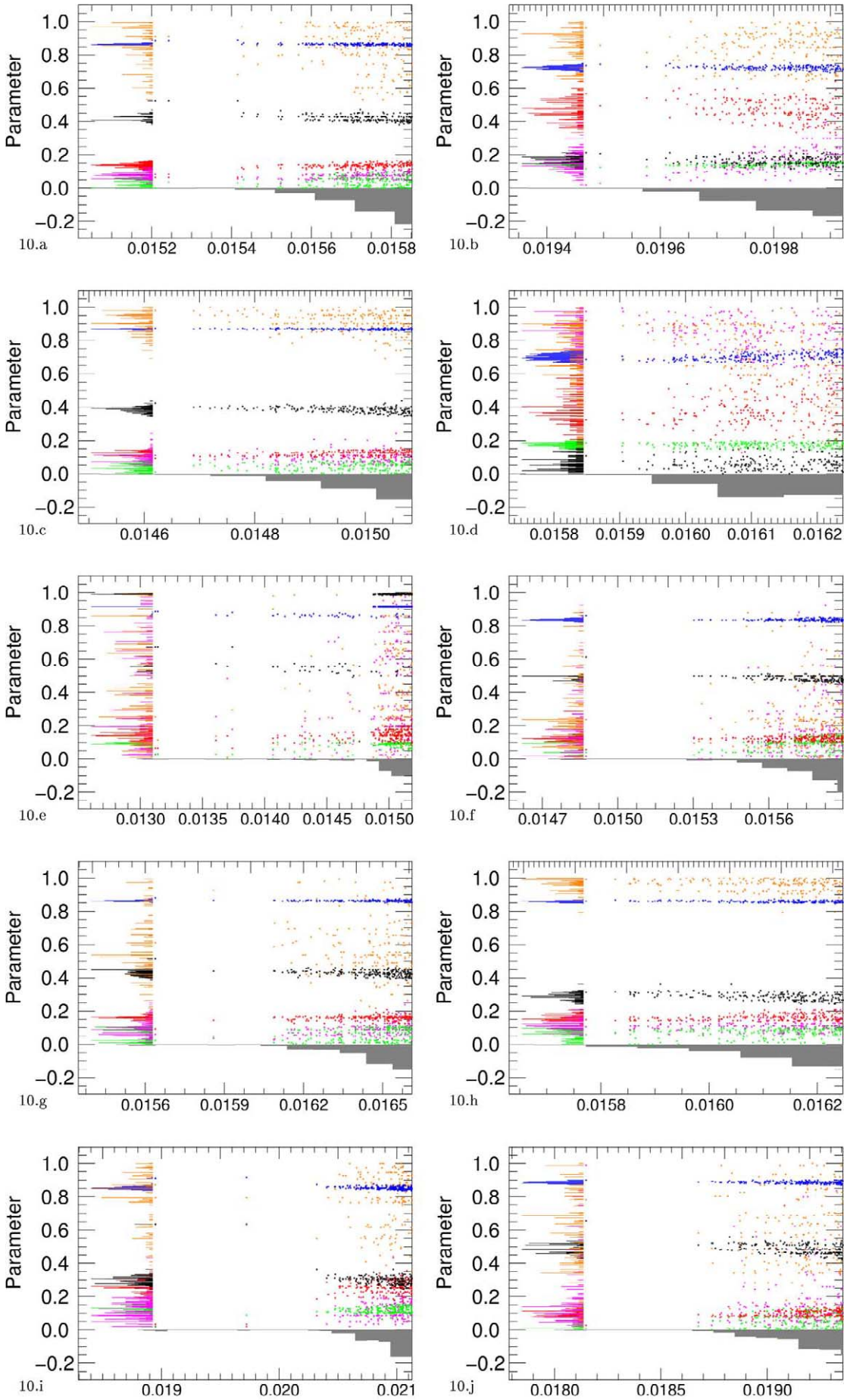

Figure 10

I10384_Fig10

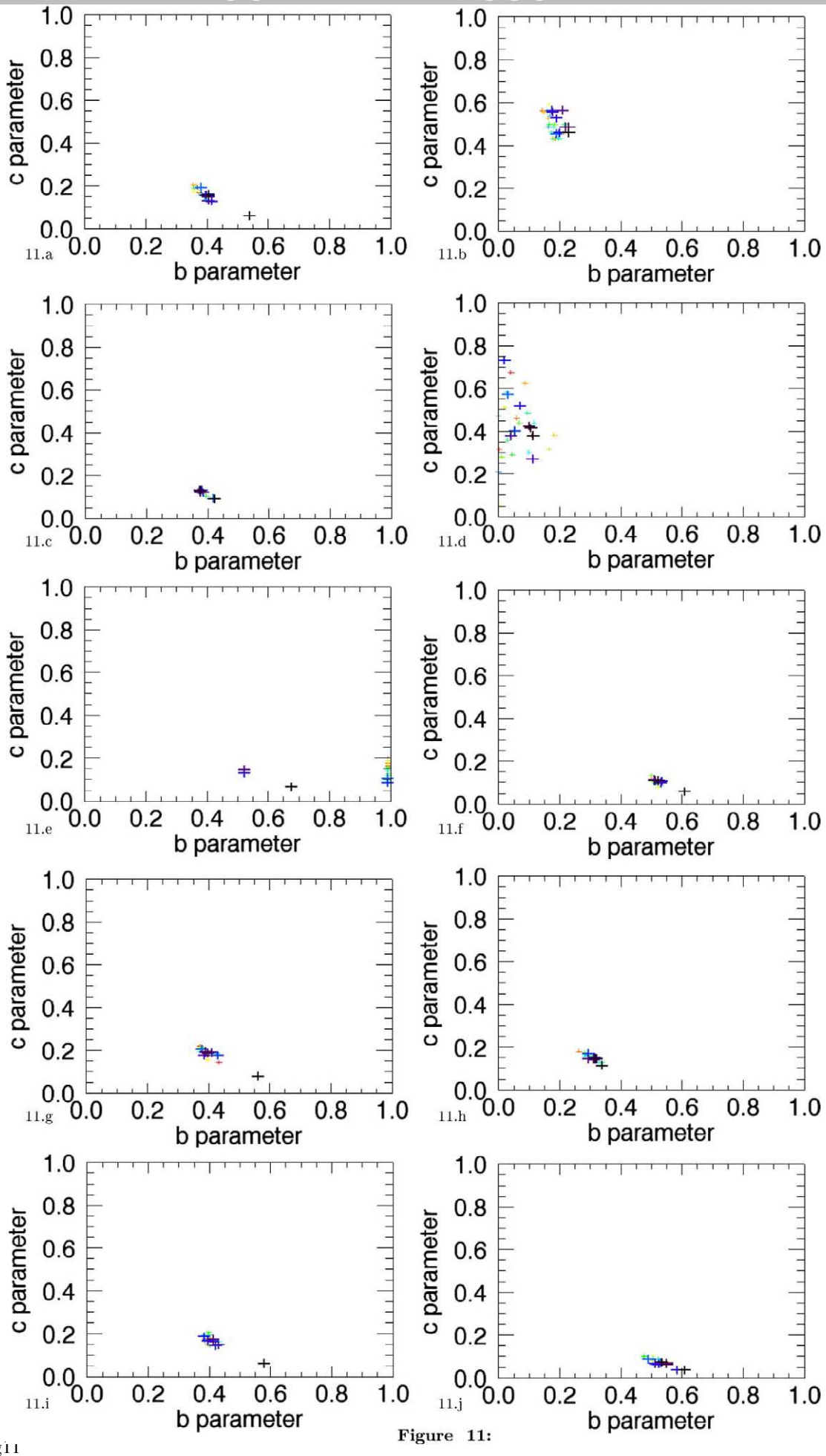

Figure 11:

I10384_Fig11

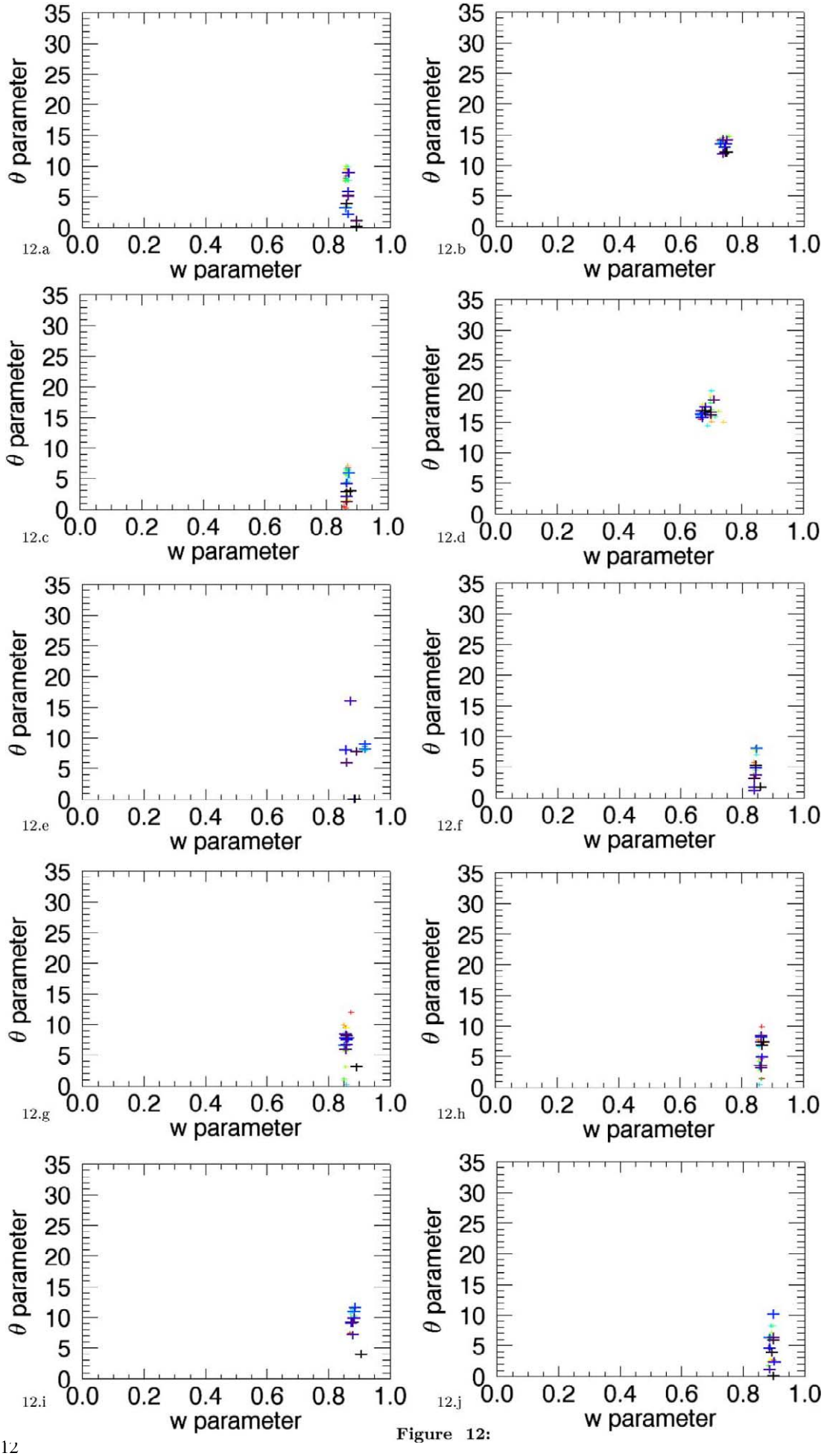

Figure 12:

I10384_Fig12

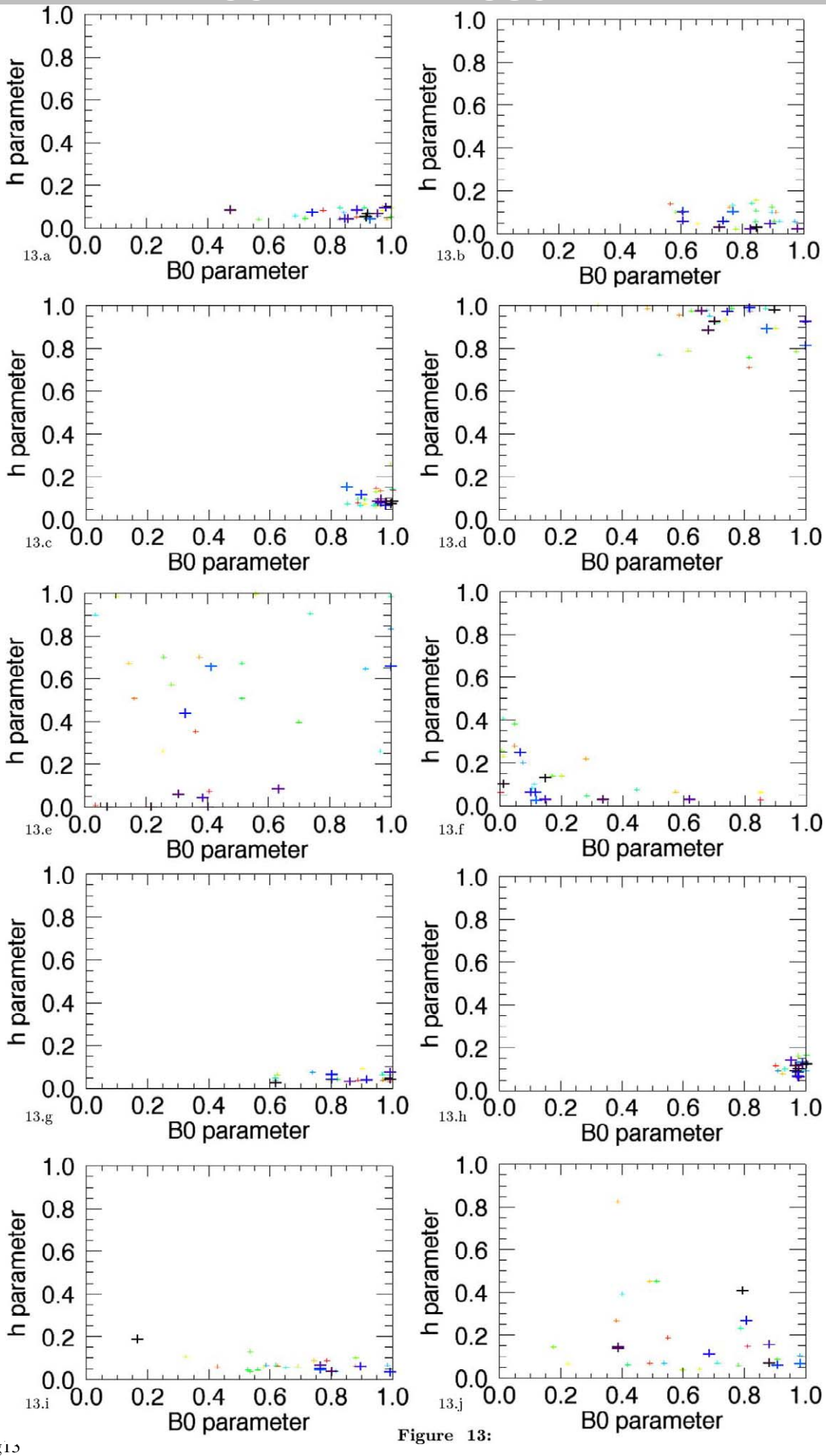

Figure 13:

I10384_Fig13

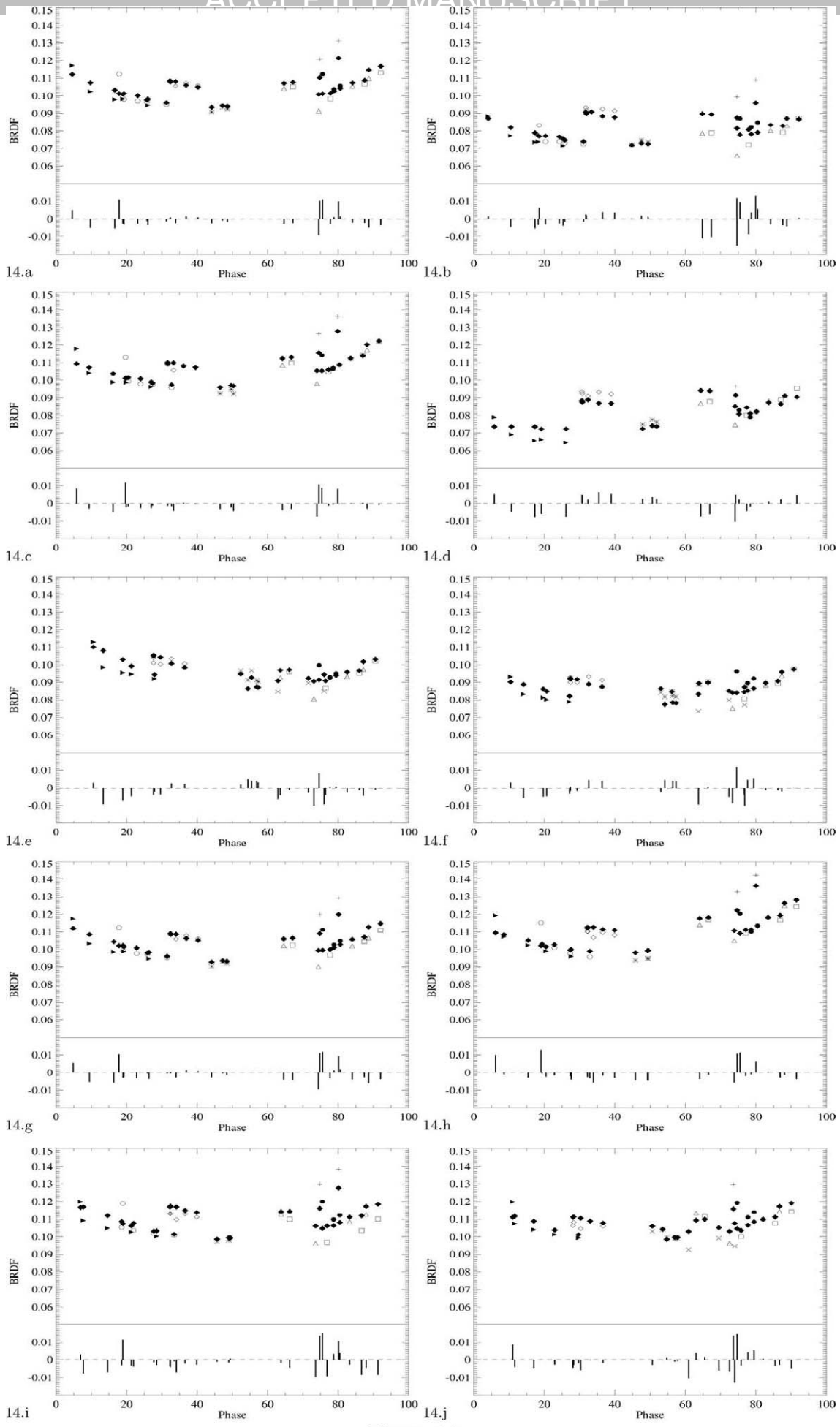

I10384_Fi

Figure 14:

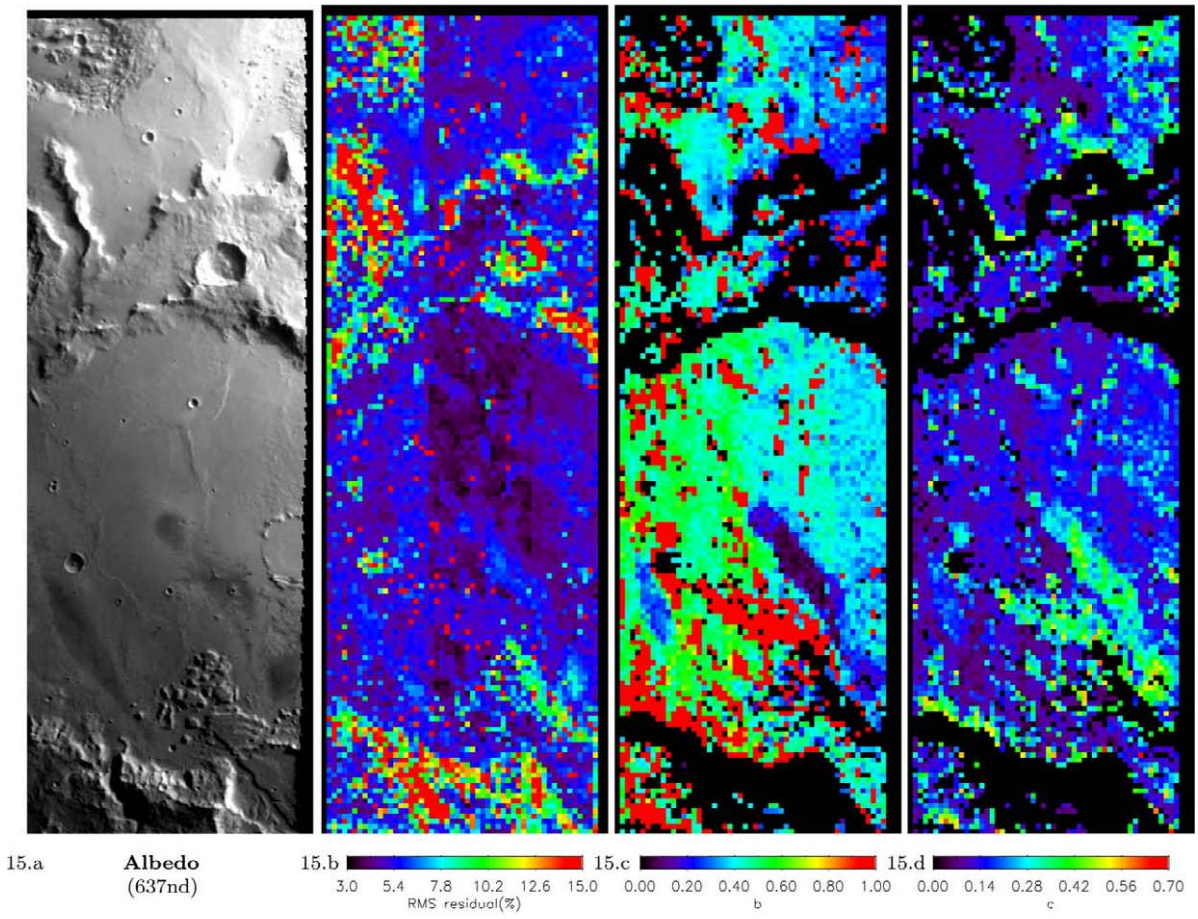

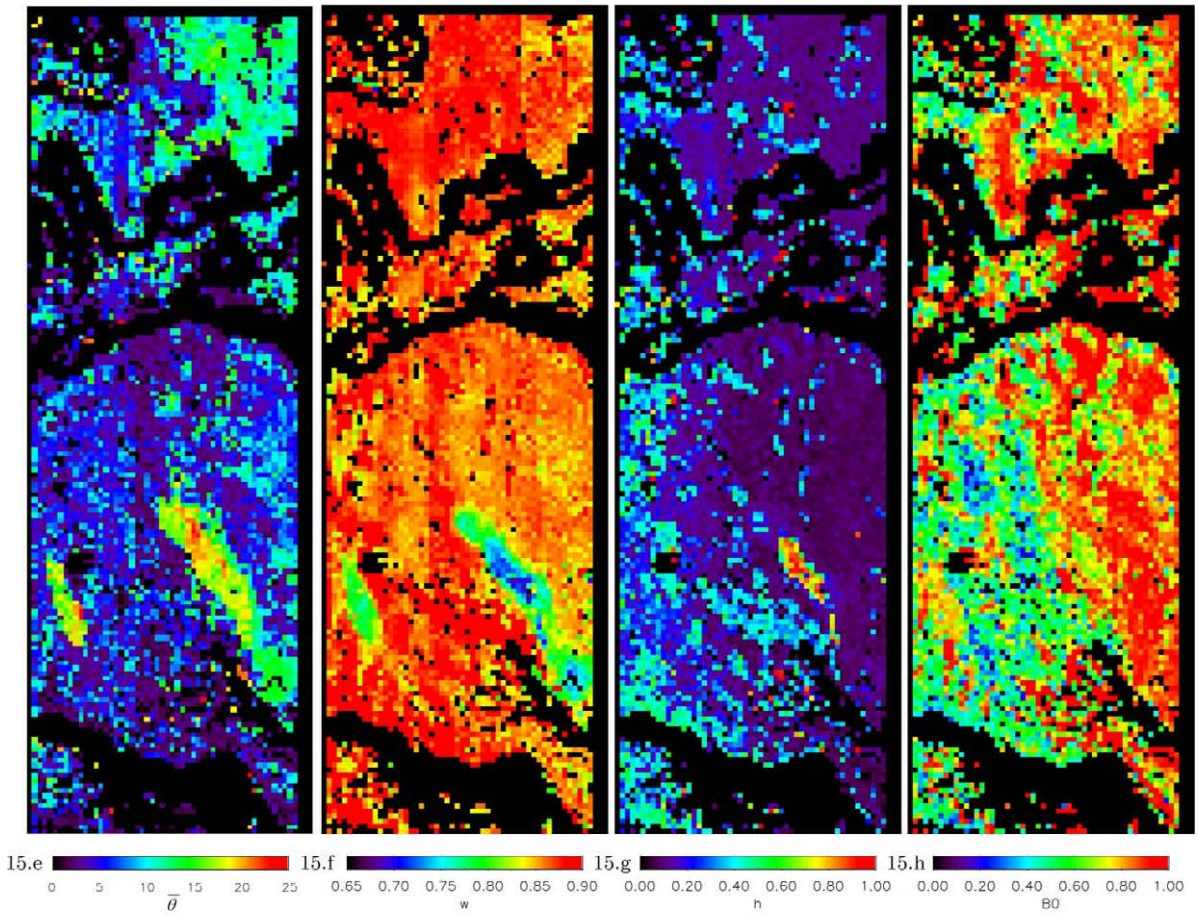

Figure 15:

I10384_Fig15

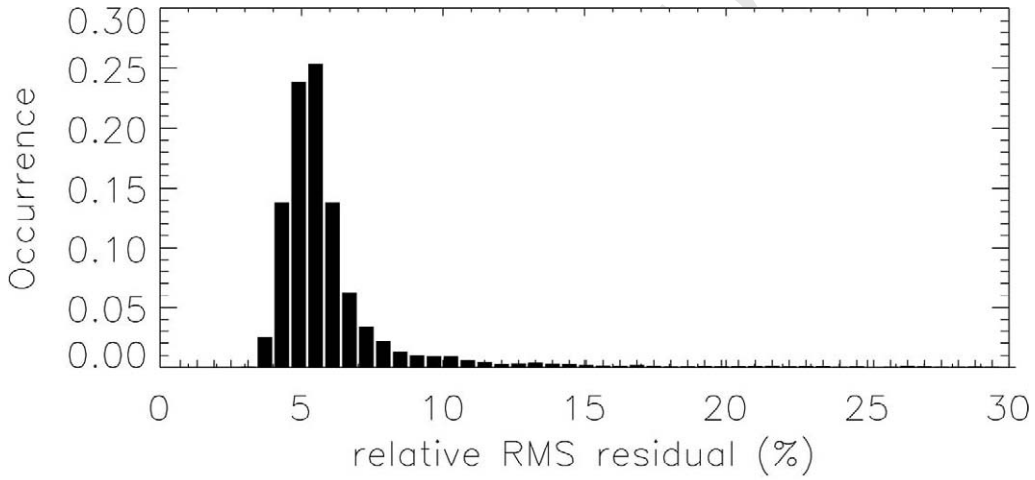

Figure 16:

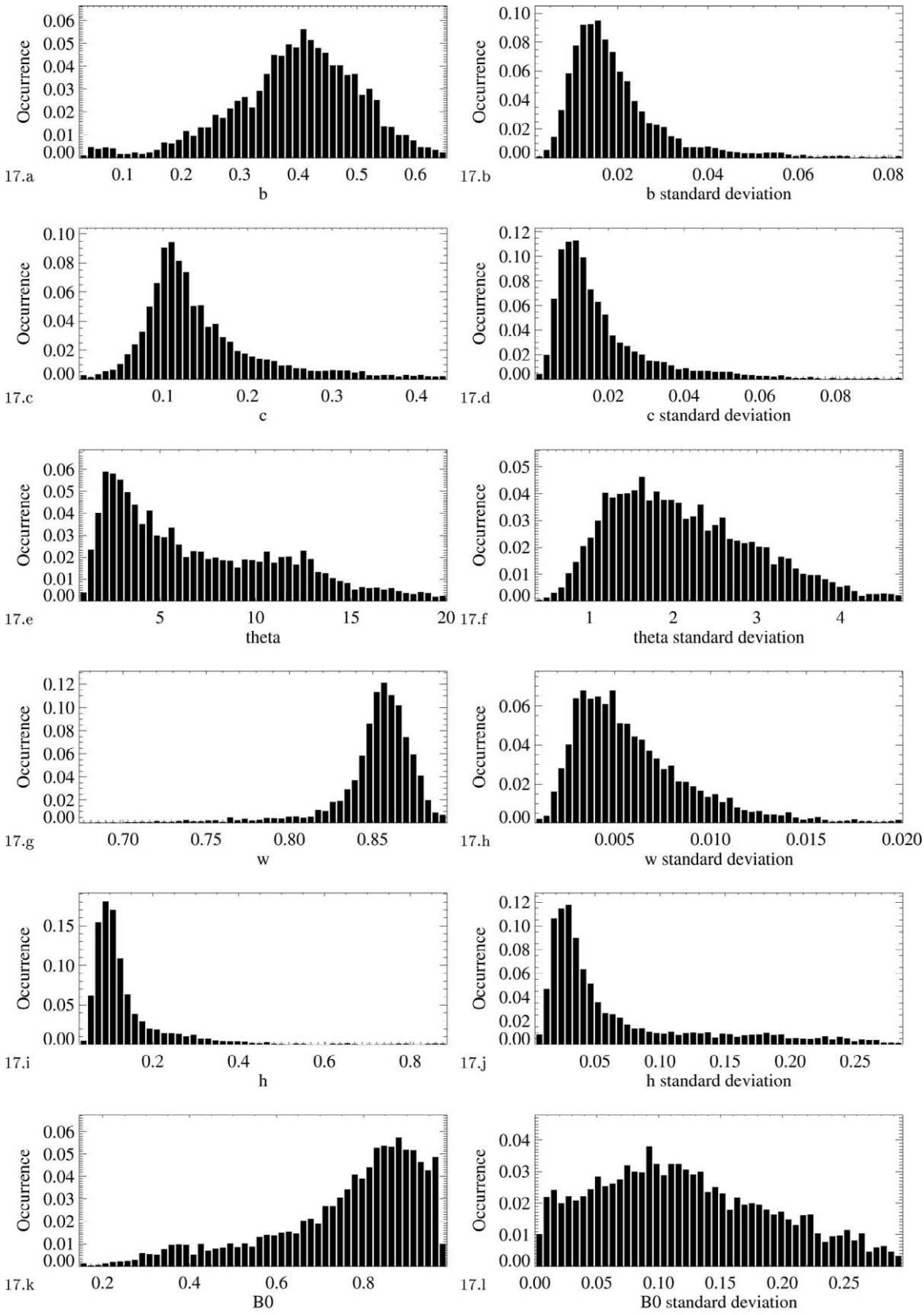

Figure 17:

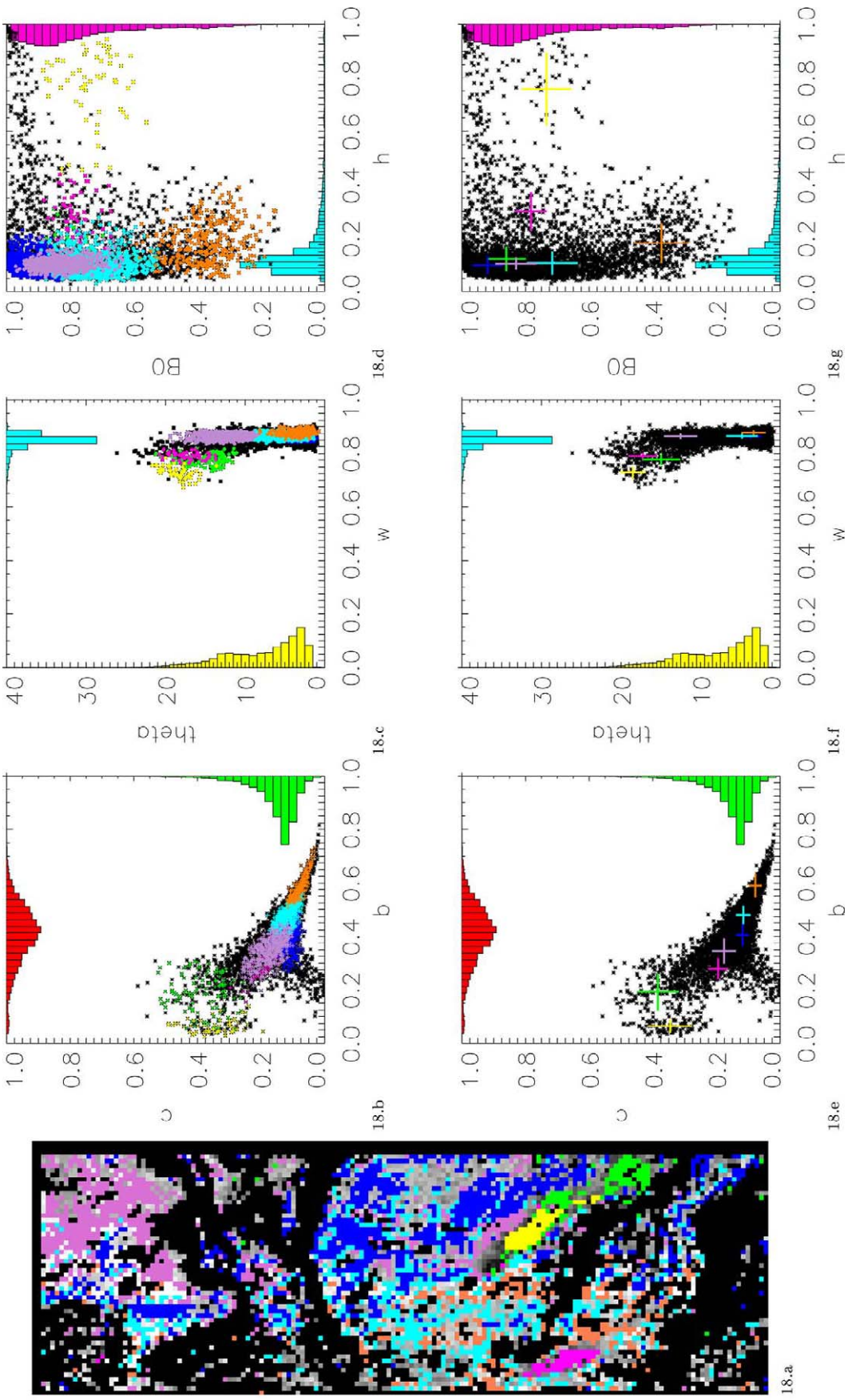

Figure 18:

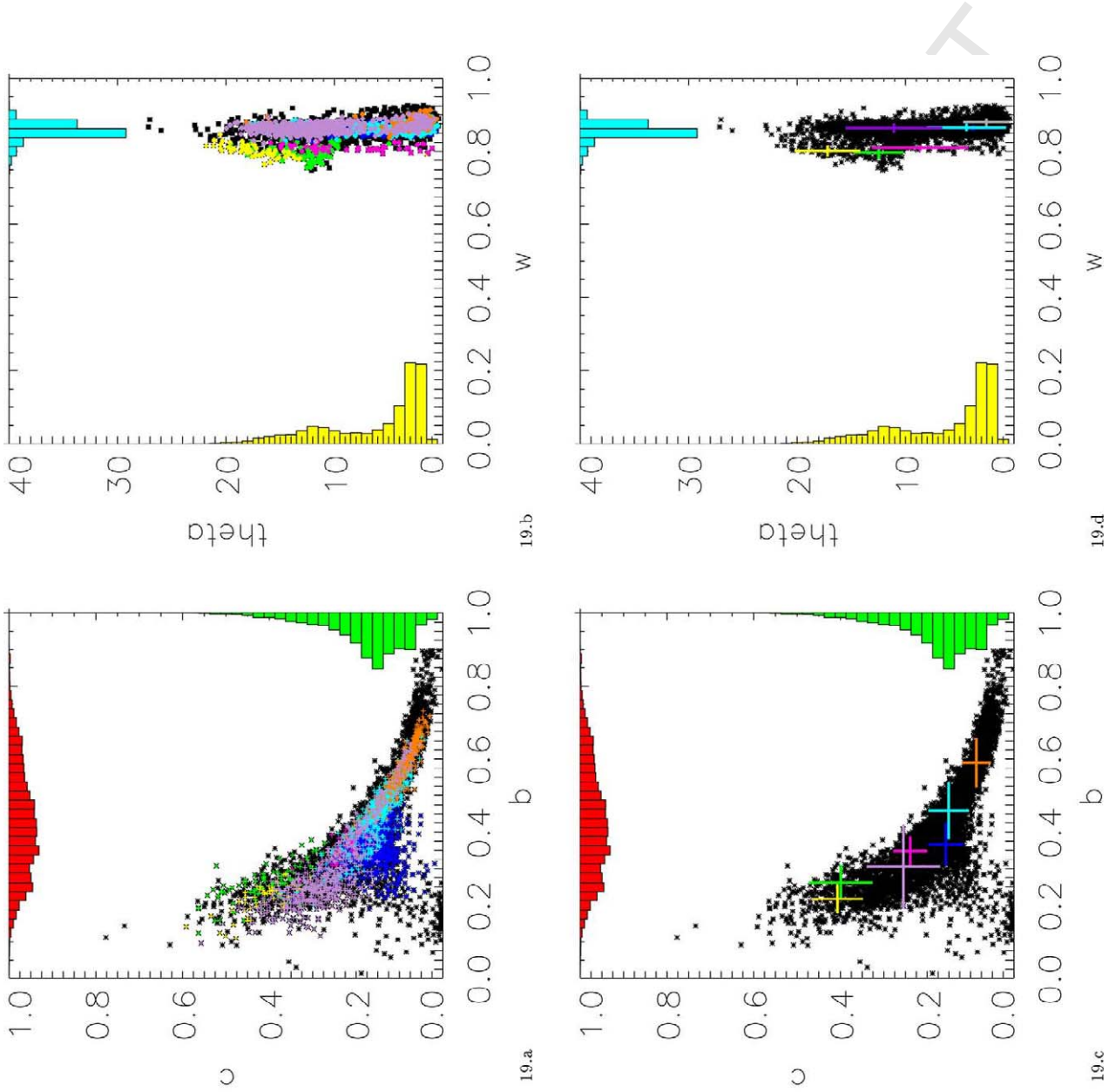

Figure 19:

Name	Acquisition Time	Ls (°)	Sub Solar Latitude	Sub Solar Longitude	τ
h0024_0000	16 Jan. 2004	334	-10.6 °	153.2 °E	0.9
h0072_0000	01 Fev. 2004	342	-7.1 °	154.1 °E	0.8
h0637_0000	20 Jui. 2004	63	22.2 °	-109.8 °E	0.3
h0648_0000	23 Jui. 2004	64	22.5 °	-109.7 °E	0.3
h0987_0000	26 Oct. 2004	106	24.2 °	119.8 °E	0.3
h1879_0000	02 Jui. 2005	241	-22.0 °	94.0 °E	1.3
h2249_0001	14 Oct. 2005	306	-20.1 °	171.9 °E	0.8
h2271_0000	20 Oct. 2005	309	-19.1 °	174.5 °E	0.8
h2685_0000	13 Fev. 2006	11	-4.7 °	-115.8 °E	<0.8
h2729_0000	25 Fev. 2006	16	7.2 °	-117.6 °E	<0.8

Tab. 1

Configuration	Mean			Spirit location (175.47°E,-14.57°N)				
	e (°)	g (°)	Deviation to Spec.(°)	i (°)	e (°)	g (°)	Deviation to Spec.(°)	Azimuth (°)
h0024_0000.nd	24±4	50±3	4±2	25.7	22.2	47.9	4.2	175±2
h0024_0000.s1	32±3	53±3	25±2	25.8	30.3	50.6	25.5	131±2
h0024_0000.s2	32±3	53±3	22±2	25.6	29.9	51.8	20.9	140±2
h0072_0000.nd	53±2	30±2	78±3	25.5	54.8	30.8	79.8	15±1
h0072_0000.p1	54±2	34±2	77±3	25.4	55.6	35.5	79.1	31±1
h0072_0000.p2	54±2	30±2	79±3	25.5	56.2	30.7	81.8	0±1
h0072_0000.s1	55±2	38±1	77±3	25.3	56.7	39.0	79.2	38±1
h0072_0000.s2	55±2	31±2	81±3	25.6	57.6	32.4	83.1	7±1
h0637_0000.nd	5±1	74±1	84±2	78.6	4.6	74.1	83.1	13±4
h0637_0000.p1	22±1	83±1	85±2	79.7	21.4	83.6	83.8	99±1
h0637_0000.p2	30±1	64±1	98±2	75.9	29.6	64.4	97.7	63±1
h0637_0000.s1	31±1	88±1	90±2	80.2	31	88.2	88.6	103±1
h0648_0000.nd	2±1	77±1	81±2	78.9	1.5	77.4	80.3	12±7
h0648_0000.p1	21±1	86±1	82±2	80.1	21.1	87.1	80.7	108±1
h0648_0000.p2	31±1	66±1	97±2	75.9	30.3	66.9	96.8	68±1
h0648_0000.s1	31±1	91±1	87±2	80.5	31	91.6	85.7	110±1
h0987_0000.nd	7±2	63±2	75±2	—	—	—	—	—
h0987_0000.p1	16±1	55±2	83±2	—	—	—	—	—
h0987_0000.p2	16±1	72±2	71±2	—	—	—	—	—
h0987_0000.s1	22±1	52±2	88±2	—	—	—	—	—
h0987_0000.s2	22±1	76±2	70±2	—	—	—	—	—
h1879_0000.nd	3±2	82±2	78±3	80.6	0.6	81	80.1	144±26
h1879_0000.p1	15±1	88±2	77±3	80.7	15.2	86.6	78.6	112±1
h1879_0000.p2	13±1	77±2	87±2	80.3	15.9	75.8	88.6	72±1
h1879_0000.s1	23±1	91±2	79±3	80.8	22.6	89.4	80.8	111±1
h1879_0000.s2	24±1	75±2	93±2	80.2	24	73.5	94.9	71±1
h2249_0001.nd	12±1	19±1	9±2	—	—	—	—	—
h2249_0001.p1	18±1	27±1	9±2	—	—	—	—	—
h2249_0001.p2	19±1	20±1	22±2	—	—	—	—	—
h2249_0001.s1	24±1	32±1	16±2	—	—	—	—	—
h2249_0001.s2	25±1	24±1	28±2	—	—	—	—	—
h2271_0000.nd	3±2	8±2	7±2	5.9	0.33	5.8	5.9	89±54
h2271_0000.p1	15±1	21±1	10±2	5.9	14.4	19.1	10.9	137±3
h2271_0000.p2	15±1	11±2	20±2	5.8	14.3	10.7	19.1	41±3
h2271_0000.s1	22±1	27±1	17±2	6.0	21.5	26.2	17.7	137±3
h2271_0000.s2	22±1	18±1	27±2	5.8	21.3	17.3	25.9	41±3
h2685_0000.nd	38±1	74±1	86±2	67.9	36.7	74.3	84.7	93±1
h2685_0000.p1	50±1	80±1	97±1	—	—	—	—	—
h2685_0000.s1	58±1	83±1	106±1	—	—	—	—	—
h2729_0000.nd	9±1	75±1	59±2	66.5	10	75.2	58.4	149±2
h2729_0000.p1	13±1	78±1	59±2	67.8	13	78.4	58.5	143±2
h2729_0000.s1	18±1	80±1	62±2	68.3	18	80.2	60.6	129±1

Tab. 2:

ROIs	Units	THEMIS Thermal Inertia ($Jm^{-2}K^{-1}s^{-1/2}$)	TES Thermal Inertia ($Jm^{-2}K^{-1}s^{-1/2}$)	TES Albedo
Red	WRt	200 ± 20	192 - 245	0.24 - 0.25
Cyan	PLt	290 ± 70	192 - 245	0.24 - 0.25
Yellow	LAt	240 ± 20	186 - 347	0.16 - 0.22
Green	HTIt	400 ± 70	295 - 532	0.17 - 0. 23

Tab. 3

	Red	Green	Blue	Yellow	Cyan
b :	0.40± 0.03	0.17± 0.02	0.40± 0.01	0.07± 0.03	0.56± 0.04
c :	0.15± 0.03	0.51± 0.06	0.11± 0.01	0.35± 0.07	0.12± 0.03
$\bar{\theta}$:	2.8± 2.5	13.3± 0.7	3.6± 2.0	17.3± 1.0	6.0± 4.0
w :	0.860± 0.006	0.729± 0.009	0.870± 0.003	0.687± 0.010	0.865± 0.009
h :	0.06± 0.02	0.10± 0.04	0.10± 0.02	0.89± 0.06	0.20± 0.21
B0 :	0.87± 0.08	0.82± 0.10	0.94± 0.05	0.84± 0.09	0.34± 0.31
scoabs :	0.016	0.020	0.015	0.016	0.015
scorel :	0.046	0.078	0.042	0.065	0.053

	Magenta	Maroon	Purple	Orchid	Chartreuse
b :	0.50± 0.03	0.44± 0.02	0.31± 0.02	0.36± 0.12	0.51± 0.03
c :	0.17± 0.02	0.15± 0.02	0.15± 0.01	0.21± 0.09	0.08± 0.01
$\bar{\theta}$:	5.3± 2.4	4.2± 3.2	5.5± 3.4	10.2± 3.5	4.5± 3.3
w :	0.836± 0.008	0.865± 0.005	0.862± 0.003	0.867± 0.022	0.889± 0.005
h :	0.13± 0.15	0.06± 0.02	0.10± 0.02	0.07± 0.04	0.16± 0.20
B0 :	0.24± 0.20	0.65± 0.18	0.97± 0.02	0.84± 0.10	0.57± 0.21
scoabs :	0.016	0.016	0.016	0.021	0.019
scorel :	0.060	0.047	0.044	0.058	0.056

Tab. 4

	Red	Green	Blue	Yellow	Cyan
b :	0.37± 0.04	0.24± 0.02	0.35± 0.01	0.23± 0.03	0.65± 0.02
c :	0.19± 0.04	0.49± 0.06	0.15± 0.01	0.44± 0.04	0.09± 0.01
$\bar{\theta}$:	5.1± 3.3	12.0± 0.8	3.3± 2.0	13.7± 1.9	2.7± 1.2
w :	0.860± 0.008	0.753± 0.008	0.870± 0.003	0.771± 0.004	0.882± 0.003
scoabs :	0.019	0.020	0.019	0.017	0.014
scorel :	0.054	0.079	0.052	0.078	0.048

	Magenta	Maroon	Purple	Orchid	Chartreuse
b :	0.60± 0.01	0.413± 0.07	0.23± 0.03	0.28± 0.06	0.45± 0.04
c :	0.07± 0.01	0.190± 0.06	0.22± 0.04	0.34± 0.06	0.12± 0.03
$\bar{\theta}$:	2.4 ± 1.5	6.2± 2.7	8.4± 1.5	10.9± 2.2	5.3± 3.2
w :	0.857± 0.003	0.864± 0.013	0.862± 0.006	0.857± 0.011	0.883± 0.008
scoabs :	0.015	0.018	0.022	0.023	0.020
scorel :	0.058	0.052	0.061	0.064	0.058

Tab. 5

Cluster	Yellow	Green	Magenta	Orchid	D-blue	Cyan	Orange
b :	0.06± 0.02	0.19 ± 0.06	0.27 ± 0.03	0.34 ± 0.04	0.40 ± 0.04	0.47 ± 0.03	0.58 ± 0.04
c :	0.34± 0.06	0.38 ± 0.06	0.19 ± 0.03	0.17 ± 0.03	0.11 ± 0.02	0.11 ± 0.02	0.07 ± 0.02
$\bar{\theta}$:	18.5± 1.5	14.9 ± 2.4	17.2 ± 1.8	12.5 ± 2.0	3.7 ± 1.3	4.6 ± 1.9	3.3 ± 1.5
w :	0.72± 0.02	0.77 ± 0.02	0.79 ± 0.01	0.86 ± 0.01	0.86 ± 0.01	0.86 ± 0.01	0.87 ± 0.01
h :	0.75 ± 0.13	0.13 ± 0.04	0.30 ± 0.07	0.10 ± 0.07	0.09 ± 0.03	0.10 ± 0.04	0.18± 0.07
B0 :	0.73 ± 0.07	0.85 ± 0.06	0.78 ± 0.04	0.82 ± 0.06	0.91 ± 0.04	0.73 ± 0.08	0.37± 0.08

Tab. 6

Cluster	Yellow	Green	Magenta	Orchid	D-blue	Cyan	Orange
b :	0.22 ± 0.04	0.26 ± 0.05	0.35 ± 0.04	0.31 ± 0.11	0.37 ± 0.06	0.45 ± 0.08	0.59 ± 0.07
c :	0.41 ± 0.06	0.40 ± 0.07	0.24 ± 0.04	0.25 ± 0.08	0.16 ± 0.04	0.15 ± 0.05	0.09 ± 0.03
$\bar{\theta}$:	17.2 ± 3.0	12.4 ± 2.3	8.7 ± 4.4	11.1 ± 4.5	3.70 ± 2.4	4.3 ± 3.5	2.55 ± 2.1
w :	0.80 ± 0.02	0.80 ± 0.02	0.81 ± 0.01	0.86 ± 0.01	0.86 ± 0.01	0.86 ± 0.01	0.88 ± 0.01

Tab. 7